

JGR Atmospheres



RESEARCH ARTICLE

10.1029/2023JD039831

Special Section:

Southern Ocean clouds, aerosols, precipitation and radiation

Key Points:

- Liquid-phase precipitation retrievals show good agreement with in situ observations and feature the prevalence of light rain
- Reflectivity to rain rate relationships are developed, showing vertical dependence and sensitivity to the intermediate-sized drops
- The below-cloud precipitation phase with radar reflectivity >0 dBZ is mostly ice, while radar reflectivity <-10 dBZ is mostly liquid

Supporting Information:

Supporting Information may be found in the online version of this article.

Correspondence to:

L. Kang, kanglt@uw.edu

Citation:

Kang, L., Marchand, R. T., & Wood, R. (2024). Stratocumulus precipitation properties over the Southern Ocean observed from aircraft during the SOCRATES campaign. *Journal of Geophysical Research: Atmospheres, 129*, e2023JD039831. https://doi.org/10.1029/2023JD039831

Received 22 AUG 2023 Accepted 23 FEB 2024

Author Contributions:

Conceptualization: L. Kang, R. T. Marchand, R. Wood Formal analysis: L. Kang Funding acquisition: R. T. Marchand, R. Wood

Investigation: L. Kang, R. T. Marchand, R. Wood

Methodology: L. Kang, R. T. Marchand Project administration: R. T. Marchand, R. Wood

Resources: R. T. Marchand

properly cited.

© 2024. The Authors.

This is an open access article under the terms of the Creative Commons

Attribution License, which permits use, distribution and reproduction in any medium, provided the original work is

Stratocumulus Precipitation Properties Over the Southern Ocean Observed From Aircraft During the SOCRATES Campaign

L. Kang¹, R. T. Marchand¹, and R. Wood¹

¹Department of Atmospheric Sciences, University of Washington, Seattle, WA, USA

Abstract Precipitation plays an important role in cloud and aerosol processes over the Southern Ocean (SO). The main objective of this study is to characterize SO precipitation properties associated with SO stratocumulus clouds. We use data from the Southern Ocean Clouds Radiation Aerosol Transport Experimental Study (SOCRATES), and leverage observations from airborne radar, lidar, and in situ probes. We find that for the cold-topped clouds (cloud-top-temperature <0°C), the phase of precipitation with reflectivity >0 dBZ is predominantly ice, while reflectivity < -10 dBZ is predominantly liquid. Liquid-phase precipitation properties are retrieved where radar and lidar are zenith-pointing. Power-law relationships between reflectivity (Z) and rain rate (R) are developed, and the derived Z-R relationships show vertical dependence and sensitivity to the presence of droplets with diameters between 10 and 40 µm. Using derived Z-R relationships, a reflectivityvelocity (ZV) retrieval method, and a radar-lidar retrieval method, we derive rain rate and other precipitation properties. The retrieved rain rate from all three methods shows good agreement with in-situ aircraft estimates, with rain rates typically being quite light (<0.1 mm hr⁻¹). We examine the vertical distribution of precipitation properties, and find that rain rate, precipitation number concentration, and precipitation liquid water all decrease as one gets closer to the surface, while precipitation size and distribution width increases. We also examine how cloud base rain rate (R_{CB}) depends on cloud depth (H) and aerosol concentration (N_a) for particles with a diameter greater than 70 nm, and find that R_{CB} is proportional to $H^{3.1}$ $N_a^{-0.8}$.

Plain Language Summary Precipitation plays an important role over the Southern Ocean (SO), such as transferring water from the atmosphere to the ocean, and affecting clouds and aerosols (tiny airborne particles). This study aims to characterize SO precipitation properties using aircraft data that can count the number and size of cloud and precipitation droplets, as well as lidar and radar that measure light and microwaves respectively reflected by droplets. Using information from lidar, we can distinguish the precipitation phase, and we find that ice precipitation is more frequent when the amount of reflected energy measured by the radar (radar reflectivity) is larger than a certain threshold. We derived relationships between rain rate and radar reflectivity. We also find the precipitation properties inferred from radar and lidar data compare well with direct measurements from the aircraft, and the precipitation tends to be very light. We study how precipitation properties vary vertically, and find that as one gets closer to the surface, there is a decrease in precipitation droplet number and water, while there is an increase in the average size of droplets. We also find that rain rate depends on how thick the clouds are and the number of aerosols, consistent with theoretical expectations.

1. Introduction

Surrounding Antarctica, the Southern Ocean (SO) is the second smallest of the five ocean basins, yet it plays an outsized role in the climate system. The SO is estimated to account for about 75% of the oceanic heat uptake and about 30%–40% of the carbon uptake (Frölicher et al., 2015; Khatiwala et al., 2009), and thus act as a strong buffer against climate change. Due to the lack of anthropogenic aerosols, the SO is also a pristine environment, and it has been argued that SO observations can be used as a present-day proxy for pre-industrial conditions as regards trying to constrain anthropogenic aerosol effects (Hamilton et al., 2014; McCoy et al., 2020), which remain a large source of uncertainty in the climate projections (Bellouin et al., 2020; Lee et al., 2016). More generally, SO clouds, especially low clouds, also have attracted much research interest in recent years because of their importance to the global radiative energy budget (Bodas-Salcedo et al., 2016; Cesana et al., 2022; Trenberth & Fasullo, 2010) as well as cloud feedbacks and climate sensitivity (Mülmenstädt et al., 2021; Tan et al., 2016; Zelinka et al., 2020).

KANG ET AL. 1 of 26



Journal of Geophysical Research: Atmospheres

10.1029/2023JD039831

Supervision: R. T. Marchand, R. Wood Visualization: L. Kang Writing – original draft: L. Kang Writing – review & editing: L. Kang, R. T. Marchand, R. Wood Precipitation impacts stratocumulus behavior via complex feedbacks that operate on both macrophysical and microphysical scales (Wood, 2012), and has been found to be a key player in the transition of stratocumulus regimes, from closed cells to open cells, and the maintenance of open cells, at least in subtropical stratocumulus (Smalley et al., 2022; Wang & Feingold, 2009; Yamaguchi & Feingold, 2015). Moreover, recent studies highlight the importance of precipitation formation as a dominant sink of cloud condensation nuclei and its control on the cloud droplet number over the SO (Kang et al., 2022; McCoy et al., 2020). Despite the importance of precipitation in low clouds, many climate models and reanalysis data struggle to accurately represent precipitation, including over the SO (Zhou et al., 2021). Mülmenstädt et al. (2021) point out that precipitation biases persist in CMIP6 models, with warm clouds precipitating too frequently, thus shortening the cloud lifetime and underestimating their cooling effect. This problem is especially pernicious for the SO because the error grows in importance, with a reduction in mixed-phase clouds as the climate warms (Bjordal et al., 2020).

Due to the remoteness of SO and a general lack of surface and in situ observations, satellite observations have long been an indispensable tool to study SO precipitation. Arguably the best available source of satellite data on SO precipitation rates is provided by CloudSat (W-band radar), which has greater sensitivity to light precipitation than passive sensors (Eastman et al., 2019; Tansey et al., 2022). CloudSat has provided an unprecedentedly broad picture of SO precipitation: Ellis et al. (2009) showed that the precipitation occurrence frequency peaks around 50°-60°S; Mitrescu et al. (2010) found that the SO has a high occurrence of very light precipitation with rain rates smaller than 1 mm hr⁻¹ having a frequency of 15%; Mace and Avey (2017) using both CloudSat and Moderate Resolution Imaging Spectroradiometer (MODIS) data found that precipitation processes in SO warm clouds vary seasonally with a stronger precipitation susceptibility to cloud droplet number in winter. Although compared to other satellite measurements, CloudSat better detects light precipitation and is better able to determine the rain rate, CloudSat is nonetheless affected by ground clutter which severely corrupts the reflectivity measurements within about 750 m of the surface (Marchand et al., 2008). CloudSat precipitation retrievals are also largely limited to situations where the measured near-surface (750–1,000 m) reflectivity is larger than -15 dBZ (Haynes et al., 2009), although the precipitation is often observed falling from SO clouds with reflectivity factors less than -15 dBZ (e.g., Mace & Protat, 2018). As shown by Tansey et al. (2022), who evaluated CloudSat retrievals using surface precipitation measurements during the Macquarie Island Cloud Radiation Experiment (MICRE), the CloudSat 2C-Precip-Column product misses most precipitation with a precipitation rate less than 0.5 mm hr⁻¹. In addition, CloudSat radar reflectivity measurements provide very limited information regarding the phase of the precipitation. The current operational CloudSat precipitation products categorize precipitation into liquid, snow, or mixed phase based largely on temperature profiles extracted from ECMWF analysis and identifying melting layers, rather than any directly measured quantity.

In the face of biases and uncertainty in satellite retrievals and modeling, precipitation observations from multiple sources such as islands, ships, and aircraft provide us with an important opportunity to obtain a more detailed view of SO precipitation. Such precipitation observations were made in several recent collaborative field campaigns (McFarquhar et al., 2021), including the aforementioned MICRE during 2016-2018, the Clouds Aerosols Precipitation Radiation and atmospheric Composition over the Southern Ocean (CAPRICORN) campaign in 2016 and 2018, the Measurements of Aerosol, Radiation, and Clouds over the Southern Ocean (MARCUS) campaign during 2017-2018, and the Southern Ocean Cloud Radiation and Aerosol Transport Experimental Study (SOCRATES) during Jan-Feb 2018. For example, Tansey et al. (2022) created a 1-year "blended" surface precipitation dataset (which combines W-band radar, tipping buck and disdrometer data) for MICRE and used these data to study the diurnal, synoptic, and seasonal variability of near-surface precipitation. These authors found that total accumulation was comprised of about 74% rain, 16% ice or mixed phase precipitation, and 10% small particle precipitation (whose phase could not be determined). In a study based on the CAPRICORN datasets, Montoya Duque et al. (2022), applied a K-means clustering technique to radiosonde data to classify the atmosphere into seven thermodynamic clusters, and found that the highest occurrence of surface precipitation was associated with warm frontal clusters and high-latitude cyclone clusters (poleward of the polar front near cyclones), with warm rain dominating in the former and the largest fraction of snow in the latter. Shipborne precipitation observations from CAPRICORN have also been included along with observations from other research vessels in the Ocean Rain and Ice-Phase Precipitation Measurement Network (OceanRAIN), the first global and comprehensive along-track in-situ water cycle surface reference dataset (Klepp et al., 2018). Protat et al. (2019) used OceanRAIN data to investigate discrepancies among satellite products at high latitudes and found large latitudinal and convective-stratiform variability in the drop size distribution (DSD). Protat et al. (2019) pointed

KANG ET AL. 2 of 26

21698996, 2024, 6, Downloaded from https://agupubs.onlinelibrary.wiley.com/doi/10.1029/2023JD039831, Wiley Online Library

onditions) on Wiley Online Library for rules of use; OA articles

out that the Southern hemisphere's high latitudes stood out as regions with a systematically higher frequency of occurrence of light precipitation with rates <1 mm hr-1 Protat et al. (2019) also noted that the shape parameter μ for the precipitation drop size distribution (DSD) in high latitudes and midlatitudes ranges from -1 to 1, which is lower than the assumed μ of two or three in the Global Precipitation Measurement Mission (GPM) rainfall algorithms (Grecu et al., 2016; Seto et al., 2013). Protat et al. (2019) found that the Southern Hemisphere high latitude (-67.5° S to -45° S), along with Northern Hemisphere polar latitude bands, stood out with a fundamentally different relationship between radar observables and rainfall properties, such as radar reflectivity to rain rate (Z–R) relationship, mainly because of much lower rain rates over the SO, suggesting that specific relationships are needed for these regions.

In this study, we use data collected during SOCRATES to study the precipitation properties of austral summertime SO stratocumulus, leveraging observations from airborne W-band HIAPER Cloud Radar (HCR), High Spectral Resolution Lidar (HSRL), and in situ probes. In particular, we examine the occurrence of liquid and ice phase precipitation, and for liquid precipitation we derived precipitation properties such as rain rate, using a hierarchy of retrieval methods from simple Z–R relationships to a more complex radar reflectivity-velocity retrieval (ZV retrieval) and radar-lidar retrieval. We also apply the precipitation observations and retrievals to study the in-and-below cloud precipitation properties and rain rate dependence on cloud depth and aerosol concentration.

This paper is organized as follows: Section 2 introduces the datasets, instruments, as well as the analysis and retrieval methods used in this study. Section 3 provides a campaign overview and discusses phase partitioning. Section 4 examines Z–R relationships and liquid precipitation retrievals and compares these remote sensing data to in situ measurements. Section 5 provides a statistical summary of the liquid precipitation properties, and Section 6 explores the relationship of stratocumulus rain rate with cloud depth and aerosol concentration, ending with conclusions in Section 7.

2. Data and Methods

In this section, we introduce the data and methods that we use to characterize in-and-below cloud precipitation properties. Section 2.1 describes the SOCRATES campaign sampling strategies, remote sensors (W-band Cloud Radar, HCR, and High Spectral Resolution Lidar, HSRL), and in situ instruments. Section 2.2 describes how we use in situ data to analyze in-cloud and below-cloud precipitation properties, as well as how we estimate Z–R relationships. In Section 2.3, we describe reflectivity-velocity (ZV) and radar-lidar retrievals.

2.1. Instrumentation and Data

In this study, we use data collected during the SOCRATES campaign to study the precipitation properties of stratocumulus. The SOCRATES campaign happened in January–February 2018 (McFarquhar et al., 2021), when the NSF/NCAR Gulfstream GV aircraft conducted 15 research flights over the SO. After taking off from Hobart (Tasmania), the aircraft typically flew south at high altitude and then descended to just above cloud top for several 10's of minutes, before heading back toward Hobart. On the return, the aircraft would descend into low clouds and sample aerosols, clouds, and precipitation with a repeating series of activities that included in-, below-, and above-cloud level legs (where the aircraft flew at a nearly fixed altitude), as well as sawtooth legs (where the aircraft ascended or descended through the cloud layer). Figure S1 in Supporting Information S1 shows a schematic of the typical flight, as well as the 15 flight tracks flown during SOCRATES.

To characterize in-and-below cloud precipitation properties, we use observations from both in situ probes and remote sensors. Table 1 gives a summary of the instruments and data we use in this study, along with a primary reference. We describe how these in situ data are used in Section 2.2.

Remote sensors include a 94-GHz W-band HIAPER Cloud Radar (HCR) (Vivekanandan et al., 2015) and a 532-nm High Spectral Resolution Lidar (HSRL) (Eloranta, 2005). Based on radar and lidar moments data, we use retrieval techniques to derive precipitation properties, as detailed in Section 2.3. HCR and HSRL were deployed in previous campaigns, such as CSET (e.g., Schwartz et al., 2019). The radar and lidar data were processed by NCAR/EOL at 2 Hz (0.5 s) temporal resolution and have 19 m vertical range resolution. A description of the NCAR/EOL data processing and corrections are given in readme files that are distributed with the data (with the link in the Data Avalibility Statement). This includes a correction of radial velocity for platform motion following

KANG ET AL. 3 of 26



Journal of Geophysical Research: Atmospheres

10.1029/2023JD039831

Table 1

nstruments	Data	References
Cloud Droplet Probe (CDP)	Size and concentration of hydrometeors with a diameter between 2 and 50 µm	Lance et al. (2010) https://data.eol.ucar.edu/dataset/552.002
Two-Dimensional Stereo probe (2DS)	Size and concentration of hydrometeors with a dimension between 10 and 1,280 $\mu \text{m}.$	Wu and McFarquhar (2019) https://data.eol.ucar.edu/ dataset/552.047
Ultra-High-Sensitivity Aerosol Spectrometer (UHSAS)	Aerosols with dry diameters between 60 and 1,000 nm	DMT (2013); Sanchez et al. (2021) https://data.eol.ucar.edu/dataset/552.002
CDP, 2DS, Two-Dimensional OpticalArray Cloud Probe (2DC), and Rosemount Icing Detector (RICE)	Cloud Phase Product	D'Alessandro et al. (2022) https://data.eol.ucar.edu/ dataset/552.142
HIAPER Cloud Radar (HCR)	Reflectivity, Doppler velocity, Spectral width, Signal-to-noise ratio, etc.	Vivekanandan et al. (2015) https://data.eol.ucar.edu/ dataset/552.034
High Spectral Resolution Lidar (HSRL)	Backscatter coefficient, Particle Linear Depolarization Ratio, Extinction coefficient, etc.	Eloranta (2005) https://data.eol.ucar.edu/dataset/552.034

Note. For both CDP and 2DS data are available at 1 Hz temporal resolution. CDP data can be found in SOCRATES Navigation, State Parameter, and Microphysics Flight-Level Data. This study uses version 1.4 of this dataset. This study uses version 1.1 of the 2DS dataset, where the raw image data were processed to determine the shape/habit of each particle by the Holroyd scheme in the University of Illinois/Oklahoma Optical Probe Processing Software (UIOOPS, McFarquhar et al., 2018). Cloud Phase Product version 1.0 is also available at 1 Hz temporal resolution. The radar and lidar moments data version 3.1 were processed by NCAR/EOL and 2 Hz (0.5 s) temporal resolution and 19 m range vertical resolution. The operational specifications of HCR and HSRL are available at https://data.eol.ucar.edu/dataset/552.034.

Romatschke et al. (2021), in which corrections are applied to the nadir and zenith pointing data separately. For nadir pointing data, radial velocity was corrected following Ellis et al. (2019), where the radial velocity of the surface (assumed to be 0 m/s) is used as a reference to correct the data with a running 3rd-degree polynomial filter. A similar method is applied to the zenith-pointing data, which is the focus of this paper. But for the zenith pointing data, instead of assuming zero velocity of surface, it is assumed that the cloud top velocities from zenith pointing times are similar to those of the neighboring nadir pointing times. Specifically, cloud top velocities are first calculated for both the nadir pointing data and zenith pointing data, then the difference between the two is used to correct the bias in the zenith pointing velocity data. Figure S2 in Supporting Information S1 shows an example of the zenith-pointing velocity fields before and after the correction. Figure S3 in Supporting Information S1 shows the averaged nadir pointing and zenith pointing velocity profiles from RF13, demonstrating that correction has removed the offset in zenith pointing velocity profiles and resulted in a similar velocity profile between nadir pointing data and zenith pointing times with cloud top velocities around 0 m/s and similar vertical variations.

2.2. In Situ Measurements

2.2.1. Droplet Size Distribution and Phase

This study uses in situ measurements mainly from two particle-sizing-instruments: a Cloud Droplet Probe (CDP) and a Two-Dimensional Stereo probe (2DS) as listed in Table 1. We focus on in situ measurement from these legs (as marked in Figure S1 in Supporting Information S1): below-cloud level legs, in-cloud level legs, and sawtooth legs (which are further divided into top-half of the cloud, bottom-half of the cloud, and the below-cloud portion as described below). These in situ measurements will be used to derive reflectivity to rain rate relationships (Z–R) relationships (Section 4.1), to validate the liquid precipitation retrievals (Section 4.3), and to study in-and-below cloud liquid precipitation properties (Section 5). In our analysis, we only consider the DSD when the in situ phase identification is liquid only by using the 1 Hz SOCRATES Cloud Phase Product developed by D'Alessandro et al. (2021, 2022). The details of the phase classification are described in D'Alessandro et al. (2021), and is based on measurements from 2DS, CDP, and Rosemount Icing Detector (RICE) instruments. In brief, a multinomial logistic regression is used to identify periods when non-spherical particles (indicative of ice) are present in the

KANG ET AL. 4 of 26

2DS images, and periods with low cloud droplet number concentrations from the CDP that contains no indication of icing (due to supercooled liquid) from the RICE are likewise identified as containing ice.

We combine measurements from CDP and 2DS to create a combined droplet size distribution (DSD) by using CDP measurements for bins $<25~\mu m$ and 2DS for bins $>50~\mu m$. For drops in the intermediate size range (25–50 μm), we take the larger values of the two probes. After combining the DSD from two probes, we further averaged the DSD for different regions and flight segments. Specifically, we examine the top half of the cloud layer from sawtooth legs; the below-cloud portion of the sawtooth legs; the below-cloud level legs in 20s intervals; and in-cloud level legs in 10s intervals. For the purpose of averaging the in-situ data into these categories, we define the aircraft as in-cloud when the liquid water content was greater than 0.03 g m⁻³ (Kang et al., 2021; Wood et al., 2011). Because of the limited sampling volumes of the probes, even with averaging, there can be gaps (and large variability) in the DSD distribution for large particles (where the concentrations are sufficiently low that the probes become increasingly unlikely to observe these particles in a given 10 or 20s period). As needed, we fill gaps in the DSD by fitting an exponential curve following Comstock et al. (2004) and extrapolate DSD (out to a diameter of 2,000 μ m) to account for the contribution from larger particles.

The DSD measurements from CDP and 2DS exhibit various sources of uncertainty as regards particle droplet size and concentration, and these uncertainties propagate, influencing the accuracy of higher moments derived from the DSD (e.g., liquid water content, LWC). For CDP, common issues include undercounting errors and oversizing errors due to coincidence (Lance et al., 2010). Faber et al. (2018) demonstrated that CDP may overestimate the median diameter by 5%-15%, with errors in higher-order moments generally below 10%. Faber et al. (2018) also compared CDP-derived LWC with the Nevzorov hot-wire probe and found that LWCCDP is greater by about 20% larger than that from the Nevzorov hot-wire. Wang et al. (2020) conducted a comparison of LWC measurements between CDP and the independent King probe (a hot-wire probe) during SOCRATES, and found that LWC from two probes is broadly consistent, with a root mean square error of 0.057 g m⁻³ and correlation coefficient of 0.96. On the other hand, 2DS has large uncertainty related to the depth of field for droplets smaller than 50 µm (D'Alessandro et al., 2021). In our analysis, we primarily rely on CDP measurements for particles smaller than 50 µm when combining the DSD data from 2DS and CDP, as described earlier in this section. While the merging does introduce an uncertainty in the effective radius of about 0.5 microns (see Kang et al., 2021), the LWC is dominated by the small droplets measured by the CDP droplets, and the uncertainty in the LWC is likewise dominated by the uncertainty in the CDP. Another potential issue highlighted by O'Shea et al. (2016) is the limited sampling volume of the 2DS probe when operating at low concentrations. To address this, we mitigate the concern by averaging over 10s or 20s periods, as mentioned above.

2.2.2. Liquid Precipitation Properties

Liquid precipitation properties are derived using the DSD. For different segments, we calculated the rain rate (liquid water flux) as:

$$R = 3,600 * \frac{\pi}{6} \rho_w \int_{D_{min}}^{\infty} n(D) D^3 v_f(D) dD$$
 (1)

where ρ_w is the density of liquid water (1,000 kg m⁻³), D is the diameter in m, the 3,600 (units of second/hour) is a scaling factor to convert the units of rain rate from kg m⁻² s⁻¹ to mm hr⁻¹, and $v_f(D)$ is the terminal fall velocity (units of m s⁻¹) of droplets in the range from D to D + dD, and n(D) is the drop size distribution (units of m⁻³ mm⁻¹). We use the terminal fall velocity model of Beard (1976) for $v_f(D)$ term. D_{\min} is the lower limit for the integration, and except where stated otherwise is set to 40 μ m. In Section 4.1, we test the importance of smaller droplets with diameter smaller than 40 μ m on the total liquid water flux (LWF_{total}).

Similarly, precipitation number (N_{precip}) is calculated as:

$$N_{precip} = \int_{D_{min}}^{\infty} n(D) \, dD \tag{2}$$

Precipitation liquid water content (LWC_{precip}) is calculated as:

KANG ET AL. 5 of 26

21698996, 2024, 6, Downloaded from https://agupubs.onlinelibrary.wiley.com/doi/10.1029/2023JD039831, Wiley Online Library on [26/03/2024]. See the Terms and Co

$$LWC_{precip} = \frac{\pi}{6} \rho_w \int_{D_{min}}^{\infty} n(D) D^3 dD$$
 (3)

Precipitation liquid water content weighted mean diameter (D_{precip}), which can be thought of as diameter at which half of LWC_{precip} is below and half is above, is calculated as:

$$D_{precip} = \frac{\int_{D_{min}}^{\infty} n(D) D^4 dD}{\int_{D_{min}}^{\infty} n(D) D^3 dD}$$

$$\tag{4}$$

Precipitation liquid water content weighted width (σ_{precip}) is calculated as:

$$\sigma_{precip} = \sqrt{\frac{\int_{D_{min}}^{\infty} n(D) D^3 (D - D_{precip})^2 dD}{\int_{D_{min}}^{\infty} n(D) D^3 dD}}$$
 (5)

2.2.3. Z-R Relationships

To estimate the Z–R relationships from in situ measurements, we calculated radar reflectivity Z and rain rate R, respectively from the in situ droplet size distributions (DSD). Rain rate is calculated as Equation 1. Reflectivity is proportional to the sixth moment of the DSD:

$$Z = \int_{D_{min}}^{\infty} n(D) D^6 \gamma_f(D) dD \tag{6}$$

where n(D)dD gives number concentrations from diameter D to D+dD, $\gamma_f(D)$ is the Mie-to-Rayleigh backscatter ratio (shown in Figure S4 in Supporting Information S1, which is the ratio of the backscatter efficiency of Mie scattering for W-band (94-GHz), calculated using the miepython package (Prahl, 2023) based on Wiscombe (1979), and backscatter efficiency of Rayleigh scattering (Bohren & Huffman, 1983). With calculated reflectivity and rain rate from the in situ DSD, the Z-R relationship assumes a traditional power-law of the form:

$$Z = aR^b (7)$$

where a and b are coefficients, and Z is the independent variable. Equation 7 can also be rearranged as $R = (Z/a)^{1/b}$, which can be used to derive R based on Z observations. Coefficients a and b can be estimated using the least-squares regression in log space following Comstock et al. (2004):

$$logR = \frac{1}{h} \left(-log \ a + log \ Z \right) \tag{8}$$

We estimated the uncertainty in estimated exponents b and intercepts a that are based on in situ data using bootstrapping. Note that in Section 4.1, we also estimated Z–R relationship based on radar observed reflectivity factor and rain rate from radar-lidar retrieval (more details in Section 2.3.3), where we use a moving blocks bootstrapping method following Wilks (1997) to estimate the uncertainty in a and b coefficients, with a block length that is close to the e-folding length.

2.3. Precipitation Retrievals Based on Remote Sensors

Precipitation retrievals described in this section use the zenith-pointing data collected when the aircraft was flying level-legs below the cloud. To illustrate, Figure 1a shows the flight track altitude and measured radar reflectivity for research flight 13 (RF13). In panel (a), the potions of the flight track which feature below-cloud-level legs are colored blue. Figures 1b–1f shows the radar and lidar data in more detail, for the below-cloud level leg starting from 03:40 UTC, which is marked by the gray shading in Figure 1a. In general, retrievals undertaken for below-cloud level legs have the advantage that the zenith pointing lidar data allows one to determine the position of cloud base, as well as providing measurements of the backscatter (Figure 1c) and depolarization ratio (Figure 1d) of the

KANG ET AL. 6 of 26

21698996, 2024, 6, Downloaded from https://agupubs.onlinelibrary.wiley.com/doi/10.1029/2023JD039831, Wiley Online Library on [26/03/2024]. See the Terms and Conditions (https://onlinelibrary.wiley.com/doins) on Wiley Online Library for rules of use; OA articles are governed by the applicable Creative Commons Licenses

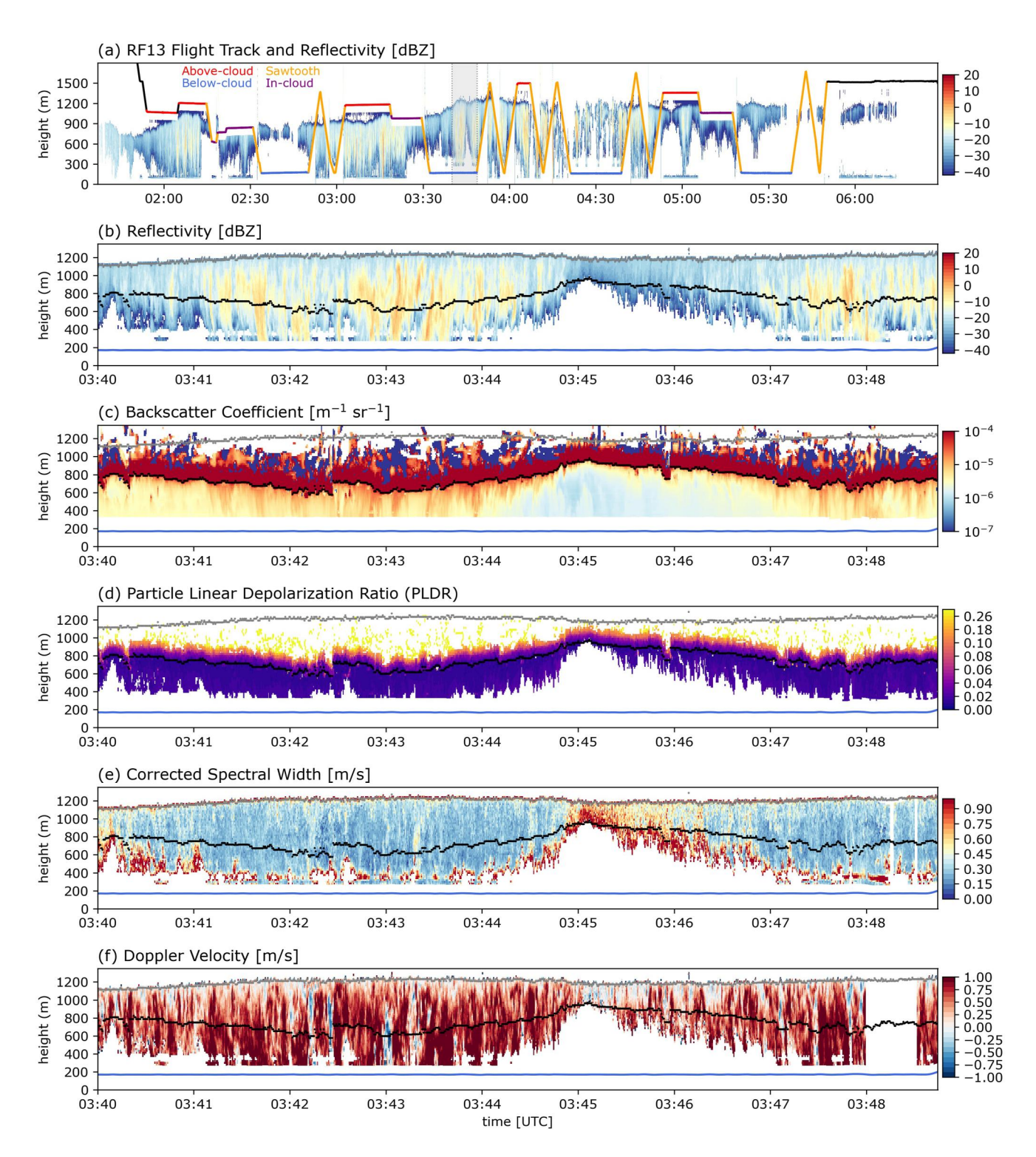


Figure 1. Example radar and lidar data collected during the SOCRATES. Panel a shows the flight tracks and reflectivity fields from research flight 13 (RF13), with different segments color-coded as in Figure S1 in Supporting Information S1. The gray shading in panel a marks a portion of one below-cloud level leg, and a zoom-in view of the radar and lidar fields for this segment are shown in panels (b)–(f): (b) radar reflectivity; (c) lidar backscatter coefficient; (d) lidar particle linear depolarization ratio; (e) radar spectral width; (f) radar doppler velocity. The gray lines show the estimated cloud top, the black lines show the estimated cloud base, and the blue lines show the location of the aircraft for below-cloud level legs.

KANG ET AL. 7 of 26

precipitation that has fallen from the cloud and can be used to determine the precipitation phase. We describe the retrieval process in the three subsections that follow: (a) determine the cloud boundaries; (b) determine the phase of precipitation; (c) determine the liquid precipitation microphysical properties (such as the rain rate).

2.3.1. Determine the Cloud Boundaries

To determine the cloud base, we use the lidar backscatter coefficient β (e.g., Figure 1c) and define the cloud base as the altitude where β first exceeds a threshold of 0.0001 m⁻¹ sr⁻¹. The black dots in Figure 1c show the cloud base identified using this threshold. Cloud top for our analysis is based on the radar reflectivity data, which have already been masked for significant detections (above the instrument noise floor). The cloud top is taken simply as the maximum height with a valid reflectivity echo (i.e., above the instrument noise floor) below 3 km, as marked by gray dots in Figures 1b-1f.

2.3.2. Determine the Phase of Precipitation Below Cloud Base

With the cloud boundaries identified, the next step is to determine the phase of the precipitation falling from the clouds. Following Mace and Protat (2018), we determine the precipitation phase using the lidar particle linear depolarization ratio (PLDR) (e.g., Figure 1d). The basic concept is that the lidar emits linearly polarized light, and scattering by spherical particles (e.g., liquid drops) does not change the polarization state of the light and thus generates little PLDR, while scattering from non-spherical particles (e.g., ice particles) creates significant depolarization and thus generates measurable increase in PLDR. In this study, for each lidar column, we examined the median of the PLDR over the vertical interval between cloud base to the first useable lidar range gate. For clouds with a cloud top temperature greater than 0°C, that is for warm clouds whose precipitation must be liquid, we find the below-cloud base PLDR values to be less than 0.03 about 90% of the time, and to be above 0.05 less than 1% of the time (see Figure S5 in Supporting Information S1 for overall statistics and Figure S6 in Supporting Information S1 for an example case). Thus, for cooler cold-topped clouds (which might precipitate ice), we define the precipitation to be liquid phase when the median PLDR <0.03; ice precipitation when PLDR >0.05; and ambiguous phase with PLDR values in between. The thresholds we use are broadly similar to Tansey et al. (2023) and Mace and Protat (2018). In Tansey et al. (2023), the liquid phase is defined with a depolarization ratio less than 0.05, and the ice phase with a value greater than 0.1. Mace and Protat (2018) defined the liquid phase with a depolarization ratio less than 0.02, and the ice phase with a value greater than 0.03. These thresholds differ somewhat because of differences in the field-of-view of the lidars used in each study, but they also represent different subjective choices for the degree of confidence desired. Our thresholds allow for little chance of a false detection of ice (nominally <1%), but consequently, some unknown fraction of ice will be identified as ambiguous. Somewhat similarly, we can expect that 10% of the cases identified as ambiguous are likely to be liquid phase. Consequently, ambiguous phase does not necessitate mixed phase (meaning both liquid and ice are present), though as we will see later, the occurrence of ambiguous phase is significantly larger than the expected 10% of failed-detection for liquid phase clouds and it is likely that many of the ambiguous cases do contain some ice phase precipitation.

We restrict our focus to the precipitation phase below-cloud, because the lidar signal becomes quickly attenuated in-cloud, and equally problematic, the depolarization ratio increases substantially in-cloud because of multiple scattering. A characterization of the phase at cloud base that accounts for multiple scattering is possible (e.g., Mace et al., 2020), as indeed is estimating vertical phase profiles using a combination of radar and lidar (e.g., Schima et al., 2022), albeit with larger inherent uncertainties.

2.3.3. Liquid Precipitation Retrieval

After determining the cloud base and precipitation phase, we can use a hierarchy of retrieval methods with increasing complexity to derive the precipitation properties, starting from (1) a simple Z–R relationship approach where only one variable, the radar reflectivity, Z, is available to derive the rain rate, to (2) a ZV retrieval following Mace et al. (2002) and Marchand et al. (2007), where radar reflectivity, Z, and mean Doppler velocity, V, are known, to (3) a radar-lidar retrieval following O'Connor et al. (2005) based on three observables: radar reflectivity Z, radar Doppler spectral width σ_d , and lidar backscatter β . We briefly describe the radar-lidar and the ZV retrieval in this section, and present retrieval results and evaluate the retrievals using in situ observations in Section 4.

KANG ET AL. 8 of 26

21698996, 2024, 6, Downloaded from https://agupubs.onlinelibrary.wiley.com/doi/10.1029/2023/D039831, Wiley Online Library on [26/03/2024]. See the Terms and Conditions

and-conditions) on Wiley Online Library for rules of use; OA articles

$$n(D) = N_w f(\mu) \left(\frac{D}{D_0}\right)^{\mu} e^{\left[\frac{-(3.67 + \mu)D}{D_0}\right]}$$
(9)

where D is diameter, and $f(\mu)$ is a function of μ

$$f(\mu) = \frac{6}{3.67^4} \frac{(3.67 + \mu)^4}{\Gamma(\mu + 4)} \tag{10}$$

where Γ is the gamma function. Integration of the droplet size distribution in Equation 9 will yield the precipitation droplet number concentration, N_{precip} , as in Equation 2.

Following O'Connor et al. (2005), one can show that for a fixed value of the shape factor, μ , the ratio of the radar reflectivity to lidar backscatter is proportional to the fourth power of the mean drop size, and the combination of radar reflectivity and lidar backscatter can therefore be used to calculate D_0 and N_w . In the retrieval algorithm, this is done assuming an initial value of $\mu = 0$. The Doppler spectral width is then forward calculated and μ is increased or decreased in order to match the observed Doppler spectral width (after applying turbulence corrections as described below). In the retrieval algorithm, we restrict μ to range from -1 to 10 following O'Connor et al. (2005). The algorithm adjusts μ and recomputes D_0 until convergence (with more details given in O'Connor et al., 2005). The forward calculations require a model for the hydrometeor terminal fall velocity, for which we use the model of Beard (1976). Once the three distribution parameters are known, it is straightforward to calculate the rain rate, rain liquid water content, and mean rain drop size, etc. using the fall velocity and Equation 9. This retrieval technique has been widely used in retrieving drizzle properties (e.g., Ghate & Cadeddu, 2019; Yang et al., 2018), including the CSET campaign with airborne radar and lidar (Sarkar et al., 2021; Schwartz et al., 2019). Our implementation largely follows O'Connor et al. (2005), except for the estimation of the contribution from air turbulence to the observed spectral width. Instead of using the horizontal wind speed to estimate the length scale, we use the aircraft speed (we note O'Connor et al. (2005) originally developed the retrieval for vertically pointing ground-based radar and lidar). Note that spectral broadening caused by aircraft motion was already corrected in the HCR data provided by NCAR/EOL, as described in Romatschke et al. (2021).

In addition to the radar-lidar retrieval technique, we also use a reflectivity-velocity (ZV) retrieval technique (Frisch et al., 1995; Mace et al., 2002; Marchand et al., 2007). The first step in this retrieval is to estimate the precipitation fall velocity from radar measured Doppler velocity, which includes the effect of vertical air motions (i.e., updrafts/downdrafts). We do this following Orr and Kropfli (1999) and partition the measured Doppler velocities into a set of height and reflectivity bins (for each below-cloud zenith-pointing segment) and average the partitioned Doppler velocity as an estimate for the fall velocity (as a function of height and radar reflectivity). The underlying idea is that at a given altitude and reflectivity, there is a characteristic size distribution (with a characteristic fall velocity) and by averaging the Doppler velocities over a narrow range of reflectivity values, one averages out the effect of the updrafts and downdrafts leaving only the mean fall velocity. In this study we use reflectivity bins are that 2 dBZ wide, and use 200 m vertical bins with 100 m overlap. The results are not particularly sensitive to these choices, as long as there is a healthy number of samples available in each bin (at least 10 samples). Following Frisch et al. (1995), it is straightforward to obtain analytical expressions for distribution parameters D_0 and N_w given the derived fall velocity, measured reflectivity, and an assumed shape factor μ . Except where we state otherwise, we assume the shape factor to be 0. One can show that the modified gamma distribution (Equation 9) reduces to the exponential distribution when the shape factor is zero. In the radar-lidar retrieval, we find the retrieved shape factor is often quite small and we will examine and discuss the sensitivity of the ZV retrieval to assumed shape factor values in Section 4.2.

KANG ET AL. 9 of 26

21698996, 2024, 6, Downloaded from https://agupubs.onlinelibrary.wiley.com/doi/10.1029/2023JD039831, Wiley Online Library on [26/03/2024]. See the Terms and Conditions

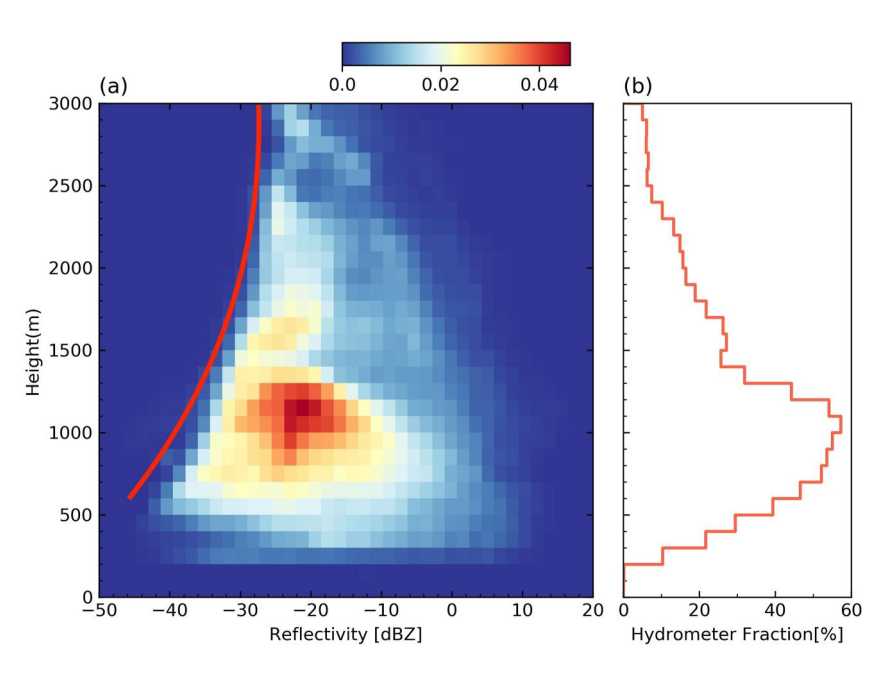


Figure 2. (a) Joint histogram of the hydrometer (cloud & precipitation) radar reflectivity with height observed by the airborne W-band radar during below-cloud, zenith-pointing periods (i.e., when aircraft is flying below the cloud, as illustrated in Figure S1 in Supporting Information S1). The histogram is normalized by the total number of radar "columns" such that the histogram values are the fractional occurrence (see text). (b) hydrometer fraction [%] at each height of all radar "columns". The red line on panel a illustrates the minimum detectable reflectivity values by HCR as a function of height.

3. Campaign Overview and Phase Partitioning

To get a general sense of the hydrometers (clouds and precipitation) sampled by the airborne W-band radar during the SOCRATES, Figure 2a shows the joint histogram of radar reflectivity with height observed during below-cloud, zenith-pointing periods. Here the histogram is normalized by the number of radar columns, such that the value in each bin indicates how often hydrometers have a reflectivity (with \pm 1 dBZ of the given value) in the given altitude/height range; and the sum at each height (row) will give the hydrometer fraction (Figure 2b).

Note that there are no data to the left of the red line in panel a. This is because of the limited radar sensitivity, and as distance increases, the minimum detectable reflectivity factor increases. Likewise, there are no data from 0 to 200 m altitude because the aircraft's lowest legs were typically flown at around 100–150 m altitude, and the radar blanking interrupt (the region corresponding to the time when the radar outgoing pulse is being, or has just been, transmitted and the radar system has not yet begun measuring the return power) typically extends about 203 m above this (Schwartz et al., 2019).

The maximum frequency of hydrometers observed by the radar occurred between 700 and 1,200 m, with a hydrometer fraction over 50% (Note this is not the projected area or the fraction of radar columns with a significant echo at any altitude, that value is near 90%). Reflectivity factors larger than -10 dBZ are relatively rare and the peak or most likely reflectivity factor is between -30 to -20 dBZ. Reflectivity factors larger than -10 dBZ are common over the Southern Ocean (see for example Mace & Protat, 2018), but such factors are associated with fronts or convection (including the shallow convection sometimes associated with vigorous open cells) and not typical of the shallow (cloud tops <2 km) and largely overcast stratocumulus sampled during SOCRATES. Rather there is a single mode or continuum of reflectivity that spans reflectivity factors from about -40 dBZ (where rain rate is very light on the order of 10^{-4} mm hr⁻¹) to values around -10 dBZ (where precipitation is still light but with a rain rate near 1 mm hr⁻¹), and a peak below -20 dBZ. We stress that rain rates near 1 mm hr⁻¹ are light but have a substantial impact on cloud condensation nuclei and cloud lifetime (Kang et al., 2022). Most of this stratocumulus are supercooled. Overall, we find that about 80% of the stratocumulus sampled during SOCRATES had a cloud top temperature <0°C and cloud depth <600 m (figure not shown), and about 62% of the stratocumulus were precipitating, defined as having three consecutive radar bins (about 60 m) below cloud base with a

KANG ET AL. 10 of 26

21698996, 2024, 6, Downloaded from https://agupubs.onlinelibrary.wiley.com/doi/10.1029/2023JD039831, Wiley Online Library on [26/03/2024]. See the Terms and Conditions (https://agupubs.onlinelibrary.wiley.com/doi/10.1029/2023JD039831, Wiley Online Library on [26/03/2024]. See the Terms and Conditions (https://agupubs.onlinelibrary.wiley.com/doi/10.1029/2023JD039831, Wiley Online Library on [26/03/2024]. See the Terms and Conditions (https://agupubs.onlinelibrary.wiley.com/doi/10.1029/2023JD039831, Wiley Online Library on [26/03/2024]. See the Terms and Conditions (https://agupubs.com/doi/10.1029/2023JD039831, Wiley Online Library on [26/03/2024]. See the Terms and Conditions (https://agupubs.com/doi/10.1029/2023JD039831, Wiley Online Library on [26/03/2024].

and-conditions) on Wiley Online Library for rules of use; OA articles

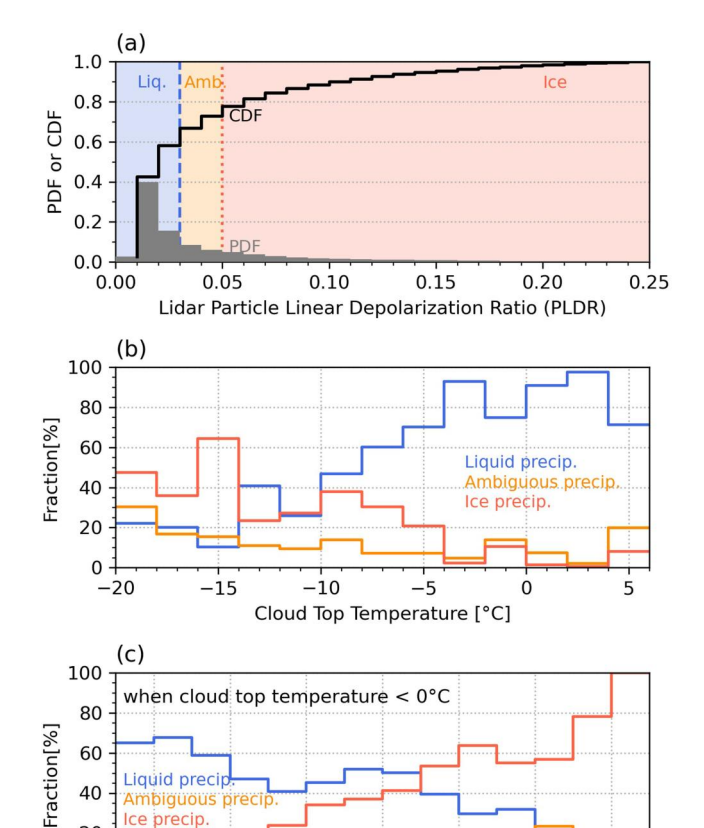


Figure 3. (a) Probability and cumulative density functions for lidar particle linear depolarization ratio (PLDR) for below-cloud precipitation, (b) The fraction of liquid, ice, and ambiguous precipitation as a function of cloud top temperature, (c) The fraction of liquid, ice, and ambiguous precipitation as a function of radar reflectivity. To distinguish different precipitation types, liquid precipitation is marked as blue, ice precipitation is marked as red, and ambiguous precipitation is marked as orange.

-10

Reflectivity [dBZ]

10

20

ce precip

-40

-30

20

reflectivity greater than -40 dBZ. This occurrence of precipitation drops to 34% if a reflectivity threshold of -20 dBZ is applied (rather than -40 dBZ), indicative of the very light nature of much of the precipitation.

What is the phase of the precipitation sampled during the SOCRATES? As described in Section 2.3.2, we determine the precipitation phase using the lidar particle linear depolarization ratio PLDR (Figure 1d), and interpret the precipitation as liquid phase when PLDR < 0.03; ice phase when PLDR > 0.05; and ambiguous for PLDR values in between. Figure 3a shows that around 60% of the precipitation from the zenith-pointing segments are liquid phase and about 20% of the precipitation are ice phase, with the remaining 20% being ambiguous phase. How does precipitation phase relate to the cloud top temperature? Figure 3b shows the relative occurrence of precipitation in different phases as a function of cloud top temperature (CTT). For the warm-topped clouds (CTT $> 0^{\circ}$ C), we expect that all the precipitation should be liquid phase. Temperature is not used in the phase retrieval, and consistent with the discussion in Section 2, the low occurrence of ambiguous or ice phase precipitation with CTT > 0° C is indicative of the low retrieval error. For the cold-topped clouds (CTT < 0°C), liquid precipitation still dominates for clouds with CTT between 0 and -10° C, with the ice fraction increasing as temperature decreases. But it is not until about a CTT of -15°C that ice phase appears to dominate.

An interesting question related to phase is whether or not precipitation phase is related to radar reflectivity. Zhang et al. (2017) have shown that lidar depolarization ratios are correlated with radar reflectivity, and for the SO in particular, Mace and Protat (2018) show that W-band radar reflectivity greater than -10 dBZ is associated with ice-phase hydrometeors (based on CAPRICORN observations). Figure 3c shows the occurrence of the different precipitation phases for cold-topped clouds as a function of reflectivity. Overall, it shows that reflectivity factors less than about -10 dBZ are predominantly liquid, while reflectivity factors greater than 0 dBZ are predominantly ice. We will discuss this result in more detail in the conclusions.

4. Liquid Precipitation Retrievals

In this section, we will explore a hierarchy of retrieval methods based on complexity, from (1) the simplest Z–R relationship approach where only one

variable reflectivity Z is known, to (2) a ZV retrieval using two variables (reflectivity Z and Doppler velocity V), to (3) a radar-lidar retrieval based on three variables (reflectivity radar reflectivity Z, doppler spectral width σ_{th} and lidar backscatter β). In Section 4.1, we will develop Z–R relationships based on in situ data. In Section 4.2, we will demonstrate the results from ZV and radar-lidar liquid precipitation retrievals using a case example, and in Section 4.3, we evaluate these retrievals using in-situ aircraft observations from all the segments where retrievals were performed.

4.1. Reflectivity to Rain Rate (Z-R) Relationships

One objective of this study is to estimate Z–R relationships of the form $Z = aR^b$. Z–R relationships are useful and convenient, requiring only one independent variable (reflectivity Z) to estimate rain rate R. Such relationships have a long history in atmospheric science, and as concerns stratocumulus in particular, relationships have been derived in past studies for stratocumulus over the Eastern Pacific (Comstock et al., 2004), over the north-east Atlantic and in U.K. coastal waters (Wood, 2005), and for nocturnal stratocumulus clouds off the California Coast (van Zanten et al., 2005). More recently, Protat et al. (2019) estimated Z-R relationships at the surface over the global ocean, including the Southern Ocean, based on surface disdrometer measurements. In this section, we will derive Z-R relationships using SOCRATES aircraft observations following the method presented in Section 2.2.3 and compare our results with previous studies.

KANG ET AL. 11 of 26

21698996, 2024, 6, Downloaded from https://agupubs.onlinelibrary.wiley.com/doi/10.1029/2023/ID039831, Wiley Online Library on [26/03/2024]. See the Terms and Conditions (https://agupubs.onlinelibrary.wiley.com/doi/10.1029/2023/ID039831, Wiley Online Library on [26/03/2024]. See the Terms and Conditions (https://agupubs.onlinelibrary.wiley.com/doi/10.1029/2023/ID039831, Wiley Online Library on [26/03/2024]. See the Terms and Conditions (https://agupubs.onlinelibrary.wiley.com/doi/10.1029/2023/ID039831, Wiley Online Library on [26/03/2024]. See the Terms and Conditions (https://agupubs.com/doi/10.1029/2023/ID039831, Wiley Online Library on [26/03/2024]. See the Terms and Conditions (https://agupubs.com/doi/10.1029/2023/ID039831, Wiley Online Library on [26/03/2024].

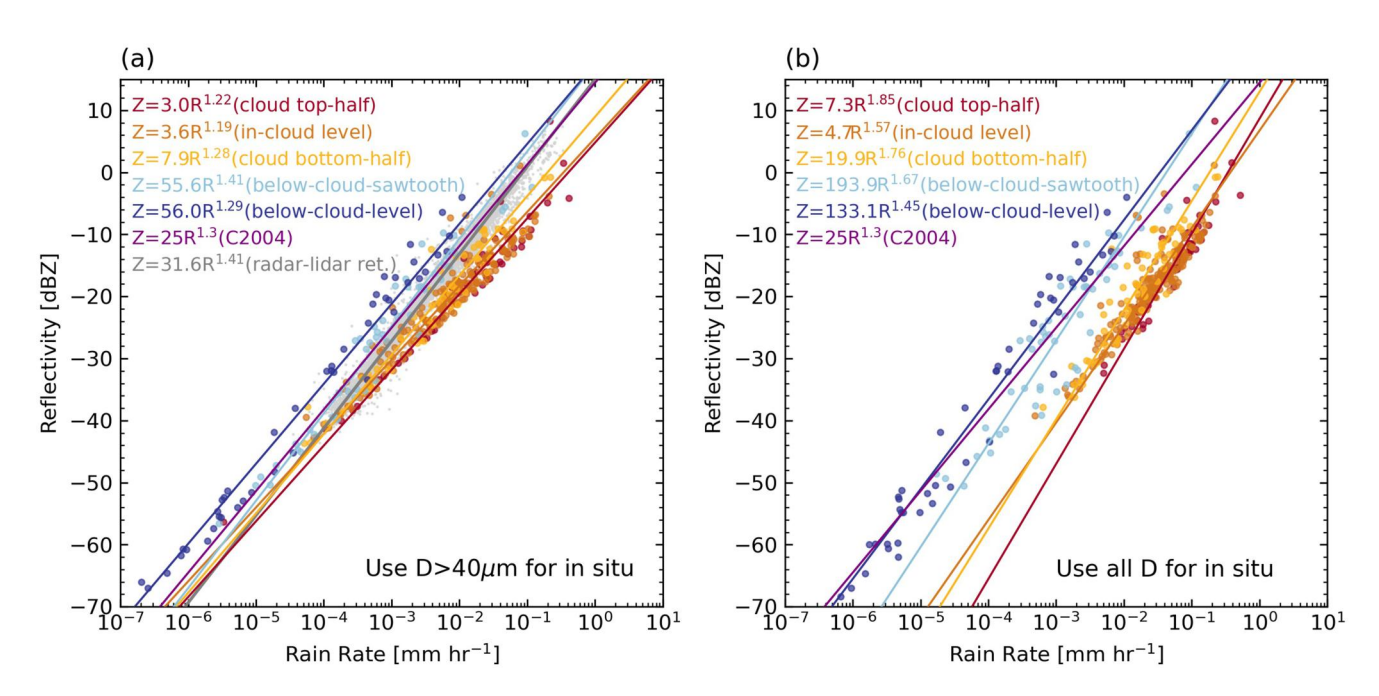


Figure 4. Z–R relationships derived using in situ data and retrievals. Diameter >40 μm cutoff for the in situ measurements is imposed in panel (a), while panel (b) does not apply any cutoff, and considers all droplet sizes for in situ data.

Figure 4 shows the Z-R relationships derived using in situ data taken at different locations relative to the cloud layer and surface (see Figure S1 in Supporting Information S1 for a schematic). Table 2 lists the corresponding a and b coefficients. In Figure 4a, we only consider droplets with a diameter larger than 40 µm following Comstock et al. (2004), while in Figure 4b, we include all droplets including those droplets with a diameter smaller than 40 μm. We will focus on Figure 4a first. Figure 4a shows that estimated Z-R relationships do have a vertical dependence. The intercept controlled by coefficient a increases as one moves from the cloud layer to the surface, while the slope controlled by exponent b remains largely unchanged. The vertical dependence of Z-R was also noticed in previous studies (e.g., Comstock et al., 2004; van Zanten et al., 2005). The exponent b estimated in Figure 4a ranges from 1.19 to 1.41, with a one-sigma uncertainty that ranges from 0.04 to about 0.07, based on a bootstrap resampling technique (uncertainties are listed in Table 2). Note the uncertainties in the a and b coefficients are not independent, but rather are positively correlated such that a larger estimate for the a-value is associated with a larger estimate for the b-values. It is worth also noting that uncertainty estimated by the bootstrapping does not account for the uncertainty in the measurements (Section 2.2.1). It only accounts for the uncertainty in the relationship given the finite sample size. As described in Section 2.2.1, this analysis includes only periods identified as liquid phase using the D'Alessandro phase product. Relaxing this restriction has no significant effect on the below-cloud values, but does result in a slight increase in the b coefficient by 0.1–0.2 and a decrease in the a coefficient by about 50% for the in-cloud relationships (given in the top three rows). Table 2 also lists some Z-R relationships estimated from other studies mentioned above. Overall, we find the exponent b to be similar to that from Comstock et al. (2004), van Zanten et al. (2005) and many other earlier studies summarized in Rosenfeld and Ulbrich (2003) over other regions and other cloud types. Later in this section, we will compare the rain rate derived from Z-R relationships with rain rate derived from two other retrieval methods.

The above analysis is based on the idea that only droplets larger than 40 μ m are considered precipitation. But droplets smaller than 40 μ m can and do contribute to the flux of liquid water (Nicholls, 1984). What happens if small droplets with a diameter smaller than 40 μ m are included when calculating Z and R from in situ DSDs? The results are shown in Figure 4b. Comparing Figures 4a and 4b, one can see that the estimated Z–R relationships are very sensitive to whether one excludes smaller drops, especially for the data collected in the cloud. Differences in the estimated Z–R are less dramatic when using in situ data outside of the cloud (i.e., below-cloud portion of the sawtooth leg and below-cloud level legs).

To explore the importance of the smaller droplets, Figure 5a shows an example of DSDs measured near the top of a cloud, near the bottom of the cloud, and below cloud during one sawtooth leg, as well as a nearby below-cloud

KANG ET AL. 12 of 26

21698996, 2024, 6, Downloaded from https://agupubs.onlinelibrary.wiley.com/doi/10.1029/2023JD098831, Wiley Online Library on [26/03/2024]. See the Terms and Conditions (https://onlinelibrary.wiley.com/doins) on Wiley Online Library for rules of user, OA articles are governed by the applicable Creative Commons Licenses

Table 2 Z-R Relationship of the Form $Z = aR^b$

Equation	Location	Remarks	Reference
$Z = (3.0 \pm 1.3)R^{(1.22 \pm 0.07)}$ $[Z = (7.3 \pm 6.7)R^{(1.85)}$ $^{\pm 0.19}]$	the top half of the cloud layer from the sawtooth leg	Estimated using SOCRATES aircraft in situ measurements with and without the 40 μ m cutoff [without given in brackets]	This study
$Z= (3.6 \pm 0.9)R^{(1.19 \pm 0.04)}$ $[Z = (4.7 \pm 1.7)R^{(1.57)}$ $^{\pm 0.08}]$	in-cloud level legs		
$Z = (7.9 \pm 2.3)R^{(1.28 \pm 0.04)}$ $[Z = (19.9 \pm 11.6)R^{(1.76)}$ $^{\pm 0.09)}]$	bottom half of the cloud layer from the sawtooth leg		
$Z = (55.6 \pm 24.6)R^{(1.41 \pm 0.05)}$ $[Z = (193.9 \pm 183.0)$ $R^{(1.67\pm0.09)}]$	the below-cloud portion of the sawtooth leg		
$Z = (56.0 \pm 45.1)R^{(1.29\pm0.05)}$ $[Z = (133.1 \pm 250.0)$ $R^{(1.45\pm0.1)}]$	below-cloud level legs.		
$Z = (31.6 \pm 1.4)R^{(1.41 \pm 0.007)}$	Cloud base	Estimated using SOCRATES W-band radar measured reflectivity and radar-lidar retrieved rain rate just below cloud base	
$Z = 25 \text{ R}^{1.3}$	Cloud base	Estimated for stratocumulus over Eastern Pacific	Comstock et al. (2004)
$Z = 12.92 \text{ R}^{1.47}$	Cloud base	Estimated using aircraft in situ DSD measurements for nocturnal stratocumulus clouds over California Coast	van Zanten et al. (2005)
$Z = 12.5 \text{ R}^{1.18}$	All in-cloud levels	Estimated using aircraft in situ DSD measurements for stratocumulus over the northeast Atlantic and in U.K. coastal waters	Wood (2005)

Note. Here uncertainty is estimated using either bootstrapping (rows 1–5) or moving block bootstrapping (row 6) with the one-sigma uncertainty given after the plus-minus sign. For the Z–R relationship that is estimated using in situ measurements, the Z–R relationship estimated using only larger droplets, with a diameter greater than 40 μ m, is listed first, followed by the Z–R relationship estimated using all droplets included those droplets with a diameter smaller than 40 μ m. For the equations above, the reflectivity Z is in the unit of mm⁶ mm⁻³, and the rain rate is in the unit of mm hr⁻¹. For the equations in the past studies with the form of $R = cZ^d$ or have different units, we rearranged the equation and converted the units to keep the consistency and make it easier to compare. Unless noted, the default band for reflectivity is W-band.

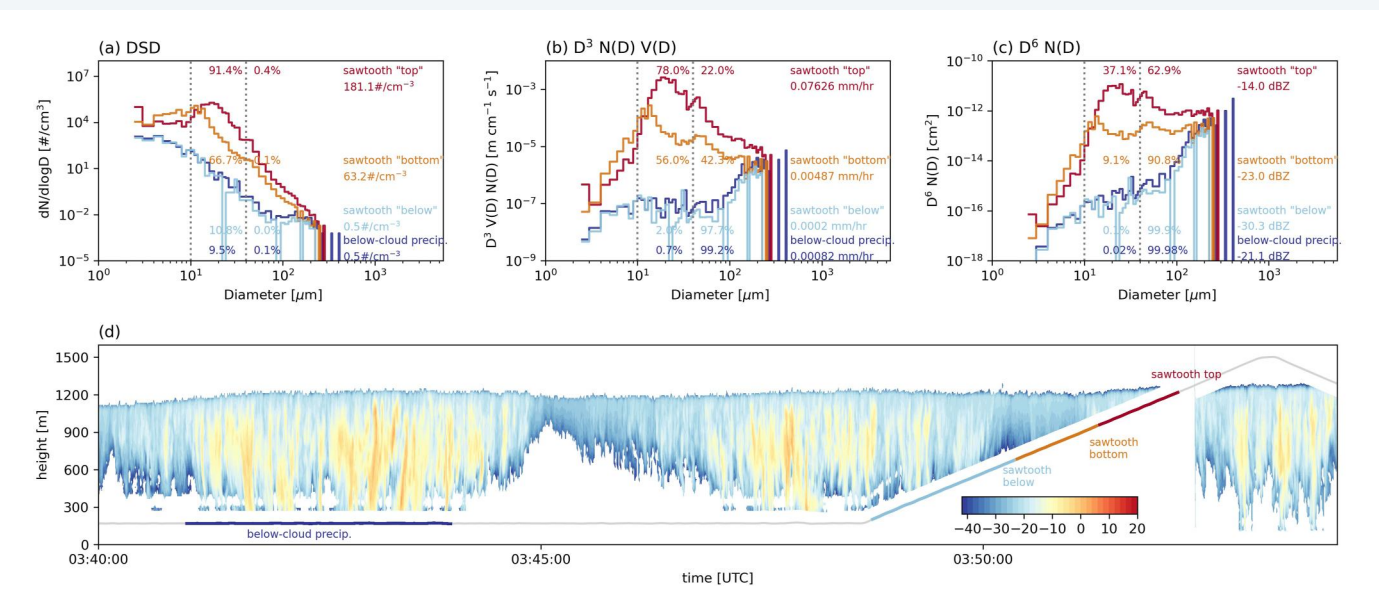


Figure 5. Example case to show the contributions of droplets in different size ranges with in situ measurements taken from different segments: (a) average droplet size distribution; (b) product of diameter cubed, droplet size distribution and terminal fall velocity; (c) product of diameter to the power of six and droplet size distribution; (d) reflectivity field and flight track for this example, the color-coded lines marked the locations of different segments showing in panel (a)–(c). The vertical dashed line in panels (a)–(c) is the reference line for 10 and 40 μ m. The percentages on panels (a), (b), and (c) show the contributions from different size ranges to droplet number concentration, to rain rate, and to reflectivity, respectively.

KANG ET AL. 13 of 26

level leg (depicted in the bottom panel). The associated liquid water flux distribution $D^3N(D)V(D)$ is shown in Figure 5b, and the reflectivity distribution $D^6N(D)$ in Figure 5c. Note as in the microphysical retrievals, here we use the terminal fall velocity model of Beard (1976) for V(D). Below cloud, small droplets evaporate much more quickly than larger droplets, and most of the contributions to the liquid water flux comes from larger droplets, such that the effect of small droplets on liquid water flux and reflectivity can be largely neglected. We hasten to add, however, this is not true for the total number concentration (Figure 5a); where small droplets remain more numerous (than droplets above $40 \mu m$), and include many particles with sizes smaller than $5 \mu m$, which one might consider haze-particles or hydrated-aerosols rather than cloud droplets. Within the cloud layer, small droplets make a large contribution to the liquid water flux, though they still only contribute slightly to the reflectivity. Droplets in the diameter range of 10– $40 \mu m$ contribute 78% of the liquid water flux in the top half of the cloud, and still comprise about half of the water flux in the bottom half of the cloud. Contributions to the reflectivity from droplets in the range of 10– $40 \mu m$ are smaller than those of larger droplets, but do make a non-trivial contribution.

In short, as Figure 5 and the differences in estimated Z–R in Figures 4a and 4b highlight, the sedimentation of small droplets is (or can be) a significant component of the total liquid water flux in cloud and applying the Z–R relationship derived from only larger particles or from below-cloud measurements effectively ignores the contribution from small particles (and below-cloud Z–R equations should be applied with caution to in-cloud reflectivity measurements and should be expected to underestimate the total liquid water flux).

It is perhaps worth noting that even below cloud, the DSD is not a simple gamma function, as assumed in the radar ZV or radar-lidar retrievals. However, as is the case in Figure 5, there is often a clear mode associated with drops larger than 40 μ m below-cloud and generally the liquid water flux and radar reflectivity (as well as the radar Doppler velocity and lidar backscatter - not shown) are controlled by these precipitation-sized drops and the gamma distribution assumption does not cause a major problem. In effect, below cloud, the gamma function only needs to represent the larger droplets. For the radar-lidar retrieval, however, this assumption is a major problem in cloud or even close to cloud base, where the lidar backscatter is substantially impacted by the cloud droplets – and ultimately, this is why we only apply the radar-lidar retrieval below cloud.

4.2. ZV Retrieval and Radar-Lidar Retrieval

In this subsection, we examine both the ZV retrieval and radar-lidar retrieval using the zenith-pointing remote sensing data collected when the aircraft was flying level-legs below the cloud. We will begin with one case study, compare results from different retrieval methods, and then examine the sensitivity of ZV retrieval results to the assumed shape factor μ . The overall retrieval performance will be evaluated in Section 4.3.

Applying the ZV retrieval (described in Section 2.3.3) to the example presented in Figure 1, the parameters D_0 and N_{precip} can be derived from measured reflectivity Z, assumed shape factor μ , and derived terminal fall velocity. Figure 6a shows the reflectivity-weighted terminal fall velocity, v_t , derived following Orr and Kropfli (1999). Here we see generally larger v_t toward the bottom of the cloud, and in precipitation shafts (regions of relatively high reflectivity extending below cloud base). Figures 6b and 6c show the derived median equivolumetric diameter D_0 , and precipitation concentration N_{precip} , assuming $\mu=0$. Not surprisingly, Figure 6b shows that D_0 is larger where v_t is larger, and is about 100–200 μ m below cloud base. Figure 6c shows N_{precip} below cloud base is in the order of 10^3 – 10^5 m⁻³.

Applying the radar-lidar retrieval technique to the example presented in Figure 1, with three input variables (radar reflectivity Z, doppler spectral with σ_d , and backscatter coefficient β), we can also solve for shape factor μ , median equivolumetric diameter D_0 , and precipitation number concentration N_{precip} , as shown in Figure 7. The shape factor μ describes the shape of the DSD (Equation 9), where a larger μ implies a narrower distribution. As in O'Connor et al. (2005), we find large areas with broad DSDs (small μ). Narrow DSDs implied by large μ are typically found underneath the thicker portion of the clouds (and as we will see later have larger rain rates). The median equivolumetric diameter D_0 is mostly between 50 and 250 μ m, with larger sizes occurring where μ is larger. Again, this is similar to what O'Connor et al. (2005) observed and appears to be quite typical for drizzling stratocumulus. Comparing the two retrieval methods, D_0 from ZV retrieval (Figure 6) tends to be more spatially homogeneous below cloud base than that from radar-lidar retrieval (Figure 7), and the D_0 from ZV retrieval tends to be smaller than that from radar-lidar retrieval in the precipitation shafts (where the assumption of a small value for the shape factor appears problematic, more on this below).

KANG ET AL. 14 of 26

21698996, 2024, 6, Downloaded from https://agupubs.onlinelibrary.wiley.com/doi/10.1029/2023JD09881, Wiley Online Library on [26/03/2024]. See the Terms and Conditions (https://onlinelibrary.wiley.com/doi/10.1029/2023JD09881, Wiley Online Library on [26/03/2024]. See the Terms and Conditions (https://onlinelibrary.wiley.com/doi/10.1029/2023JD09881, Wiley Online Library on [26/03/2024]. See the Terms and Conditions (https://onlinelibrary.wiley.com/doi/10.1029/2023JD09881, Wiley Online Library on [26/03/2024]. See the Terms and Conditions (https://onlinelibrary.wiley.com/doi/10.1029/2023JD09881, Wiley Online Library on [26/03/2024]. See the Terms and Conditions (https://onlinelibrary.wiley.com/doi/10.1029/2023JD09881, Wiley Online Library on [26/03/2024]. See the Terms and Conditions (https://onlinelibrary.wiley.com/doi/10.1029/2023JD09881, Wiley Online Library on [26/03/2024]. See the Terms and Conditions (https://onlinelibrary.wiley.com/doi/10.1029/2023JD09881, Wiley Online Library on [26/03/2024]. See the Terms and Conditions (https://onlinelibrary.wiley.com/doi/10.1029/2023JD09881, Wiley Online Library on [26/03/2024]. See the Terms and Conditions (https://onlinelibrary.wiley.com/doi/10.1029/2023JD09881, Wiley Online Library on [26/03/2024]. See the Terms and Conditions (https://onlinelibrary.wiley.com/doi/10.1029/2023JD09881, Wiley Online Library.wiley.com/doi/10.1029/2023JD09881, Wiley Online Library.wil

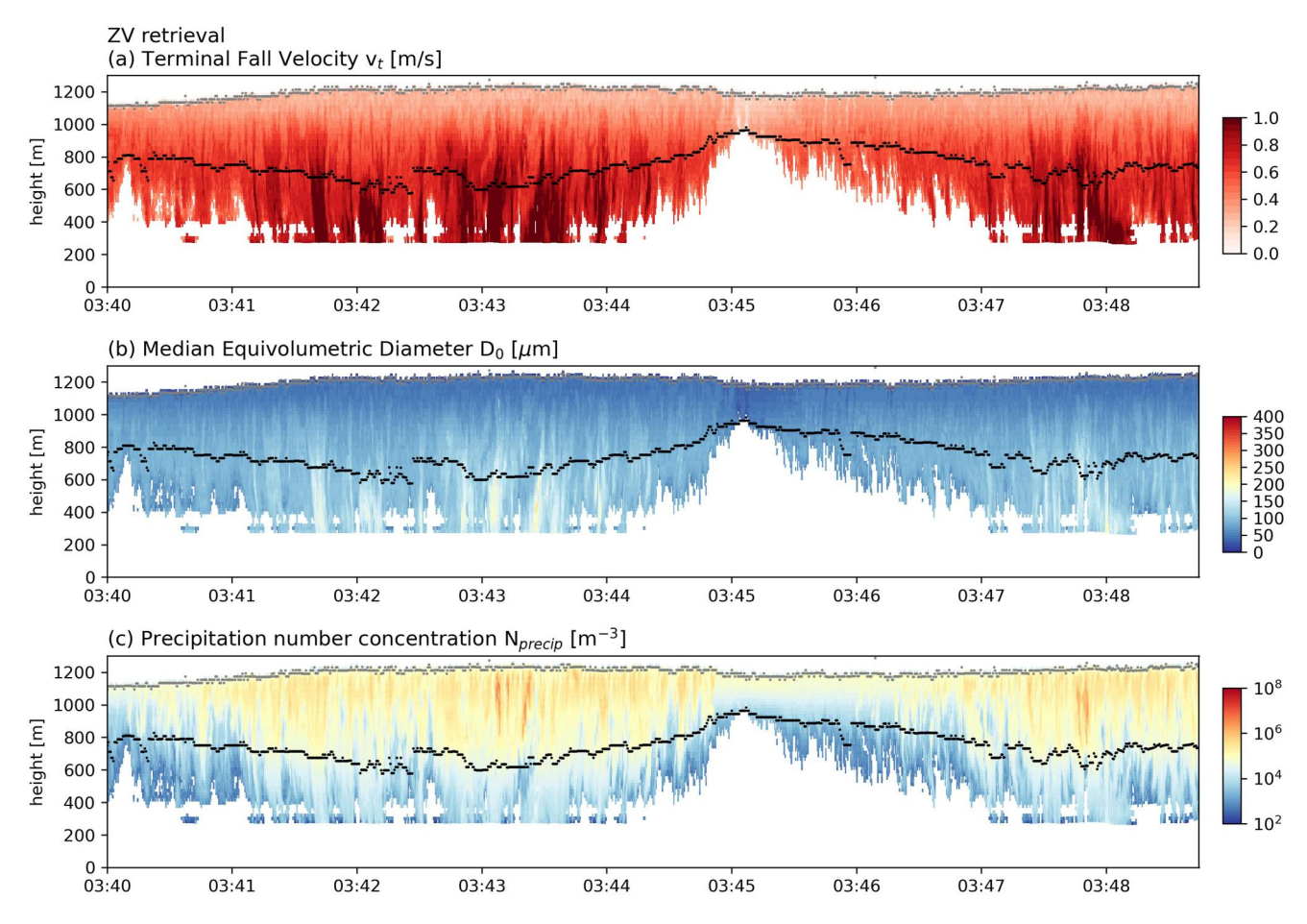


Figure 6. A time-height plot of the ZV method retrieved precipitation properties assuming a shape factor of zero for the example segment is shown in Figure 1: (a) reflectivity-weighted the terminal fall velocity v_t , (b) median equivolumetric diameter D_0 , and (c) precipitation number concentration N_{precip} . The gray lines show the estimated cloud top, the black lines show the estimated cloud base.

Once the parameters that determine the DSDs are derived, it is straightforward to calculate other precipitation properties such as rain rate. Figures 8b and 8c show the ZV retrieved the rain rate (assuming $\mu=0$) and radar-lidar retrieval retrieved the rain rate. Overall, the two retrieval methods give similar results (at cloud base, the mean rain rate from the ZV retrieval is 0.008 mm hr⁻¹, and the mean rain rate from the radar-lidar retrieval is 0.007 mm hr⁻¹). With derived Z–R relationships from Section 4.1, one can also derive rain rate by applying them to the radar reflectivity fields, as shown in Figure 8a, where we have applied three Z–R relationships: the *sawtooth-top* relationship to the top half of the cloud, the *sawtooth-bottom* relationship to the bottom half of the cloud, and the *sawtooth-below* relationship to the area below the cloud base. The discontinuity in the rain rate fields in Figure 8a is because three different Z–R relationships are applied to different regions. The difference in Z–R relationships (i.e., with or without D > 40 μ m cutoff) also results in differences in the derived rain rate (Figure S7 in Supporting Information S1), especially for the in-cloud portion. Overall, regardless of the retrieval approaches, it can also be seen that higher rain rates tend to occur below the geometrically thicker portion of the clouds, and we will explore the scaling between rain rate and cloud depth further in Section 6.

In Figures 6 and 8b, we assume $\mu=0$ in the ZV retrieval, while the retrieved μ from radar-lidar retrieval clearly shows spatial variations (Figure 7a). How does the ZV-retrieved D_0 , N_{precip} , and rain rate vary with assumed μ ? Figure S8 in Supporting Information S1 shows that the derived D_0 increases with increasing μ values such that the mean D_0 just below cloud base is 102 μ m when $\mu=0$, and is 156 μ m when $\mu=10$. When using radar-lidar retrieved μ as input for ZV retrieval, the spatial variations in retrieved D_0 (Figure S8 in Supporting Information S1) are similar to radar-lidar retrieved D_0 (Figure 7b). In contrast, as shown in Figure S9 in Supporting Information S1, the derived N_{precip} decreases significantly with increasing μ values, with mean N_{precip} at cloud

KANG ET AL. 15 of 26

21698996, 2024, 6, Downloaded from https://agupubs.onlinelibrary.wiley.com/doi/10.1029/2023JD09881, Wiley Online Library on [26/03/2024]. See the Terms and Conditions (https://onlinelibrary.wiley.com/derms-and-conditions) on Wiley Online Library for nules of use; OA articles are governed by the applicable Creative Commons Licensia

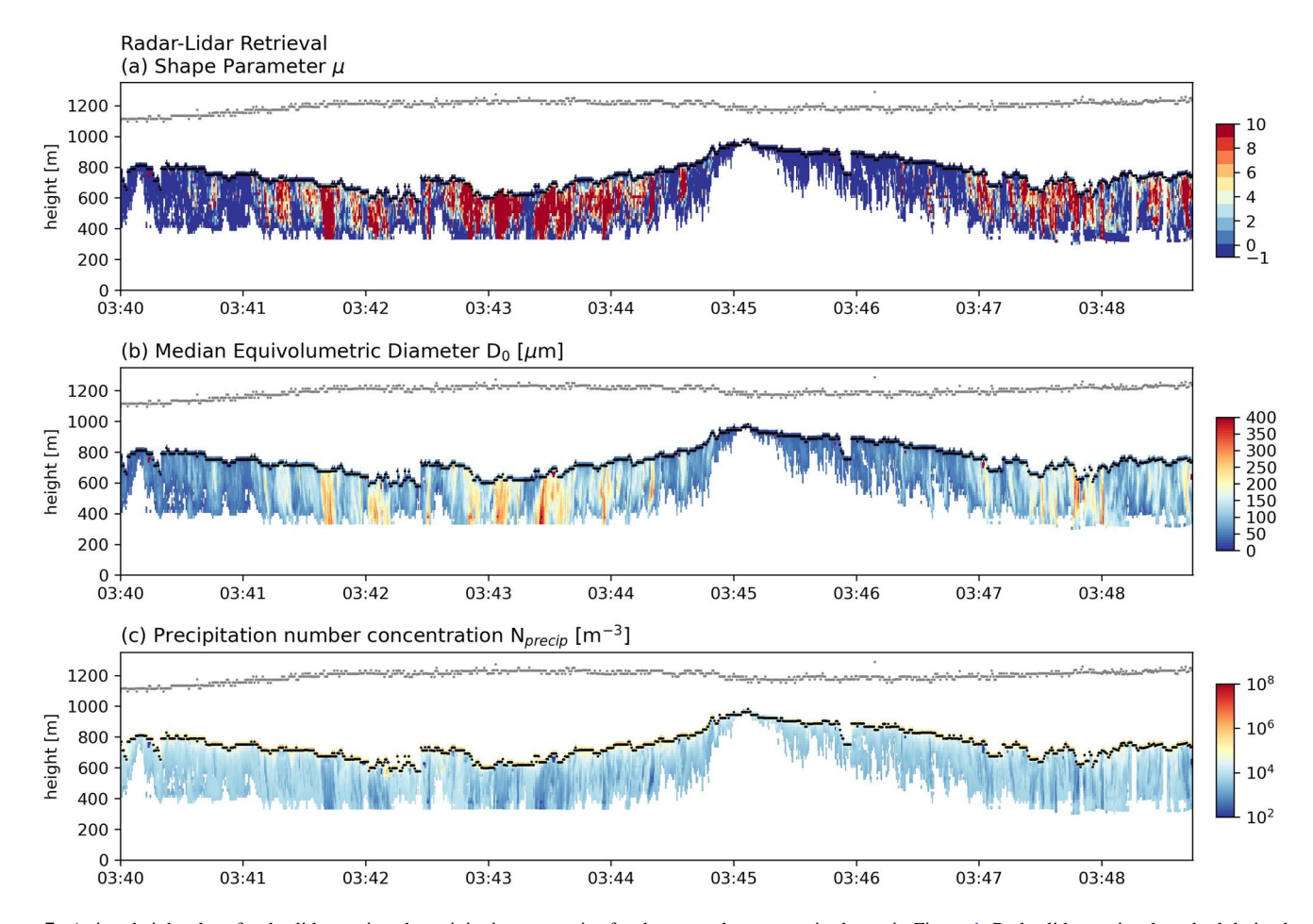


Figure 7. A time-height plot of radar-lidar retrieved precipitation properties for the example segment is shown in Figure 1. Radar-lidar retrieval method derived parameters for modified gamma distribution: (a) shape factor μ , (b) median equivolumetric diameter D_0 , and (c) precipitation number concentration N_{precip} . The gray lines show the estimated cloud top, and the black lines show the estimated cloud base.

base being about 1.3×10^5 m⁻³ when $\mu = 0$, and about 1.2×10^3 m⁻³ when $\mu = 10$. On the other hand, the derived rain rate (Figure S10 in Supporting Information S1) shows relatively little dependence on assumed μ , with the rain rate at cloud base decreasing slightly from about 0.008 mm hr⁻¹ ($\mu = 0$) to about 0.007 mm hr⁻¹ ($\mu = 10$). The small sensitivity in rain rate ultimately arises because the liquid water flux is to first order given by the velocity (which is input to the retrieval) times the liquid water content (which is strongly constrained by the reflectivity that is likewise input to the retrieval).

4.3. Retrieval Validation

How good are the rain rate retrievals? One would think a simple comparison between the retrieved rain rate with in situ measurements from the aircraft could answer this question. But there are a few challenges that need to be overcome.

The first challenge is that retrieved rain rates that are closest to the aircraft level marked as a dashed line around 200 m in Figure 8) are still at least 150 m away, making it difficult to make a direct comparison. This is because there is a blanking interrupt, a brief period where one needs to wait for the outgoing pulse to exit the radar (or lidar) system and for the effect of strong scattering from nearby objects (clutter) to dissipate. To overcome this difficulty, we extrapolate the retrieved rain rate downwards to the aircraft level by fitting an exponential function to each radar column. The assumption is that the rain rate varies with distance below the cloud base exponentially due to evaporation (Comstock et al., 2004; Wood, 2005). Figure S11 in Supporting Information S1 shows an example of rain rate derived from the exponential fit, and demonstrates that the exponentially fitted rain rate shows reasonable agreement with the retrieved rain rate where such is retrieved. Figure 8d compares the

KANG ET AL. 16 of 26

21698996, 2024, 6, Downloaded from https://agupubs.onlinelibrary.wiley.com/doi/10.1029/2023JD039831, Wiley Online Library on [26/03/2024]. See the Terms and Conditions (https://onlinelibrary.wiley.com/doin) on Wiley Online Library for rules of use; OA articles are governed by the applicable Creative Conditions (https://onlinelibrary.wiley.com/doin).

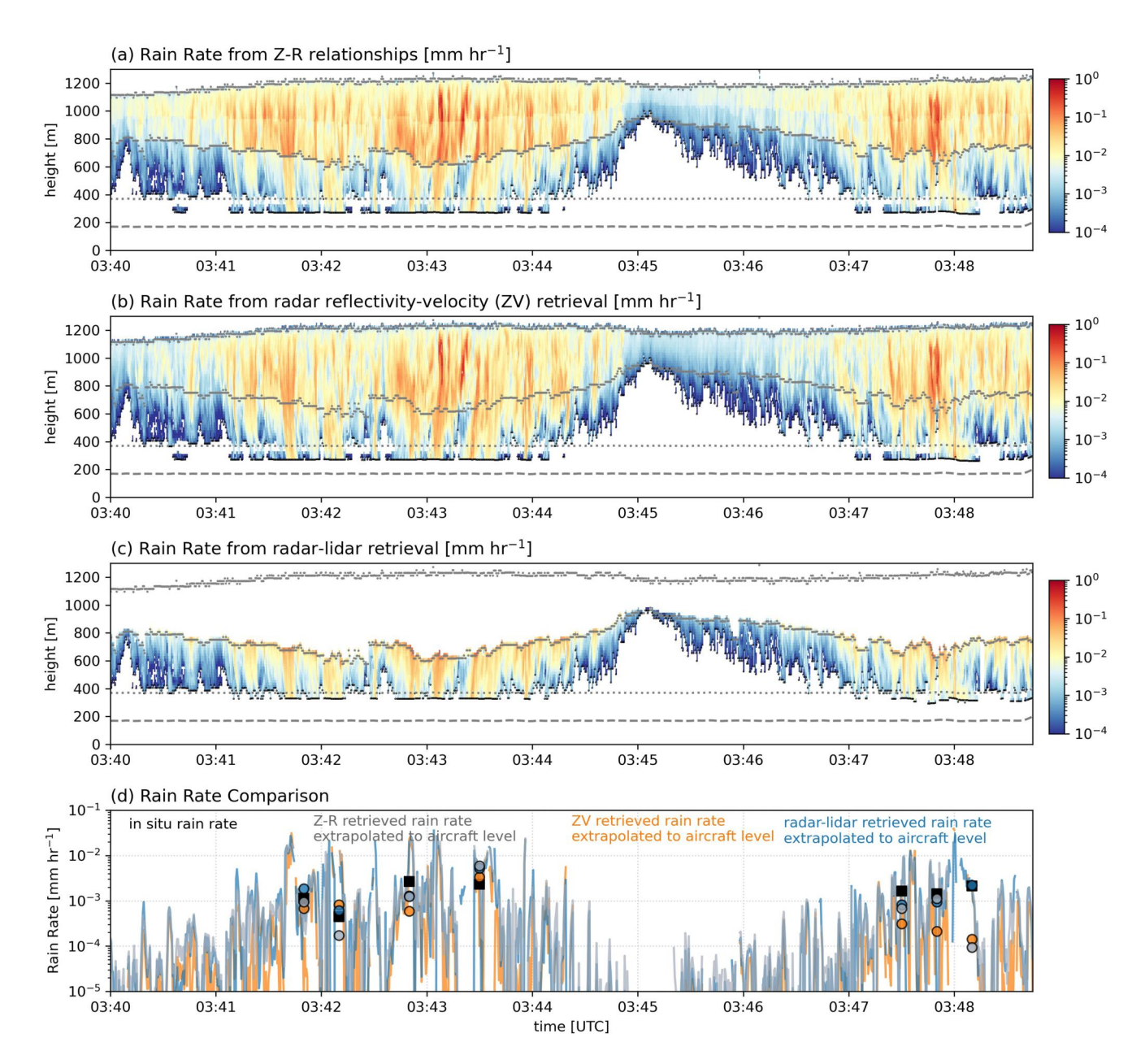


Figure 8. Retrieved rain rate for example case using (a) Z–R relationships ($D > 40 \mu m$), (b) ZV retrieval technique, (c) radar-lidar retrieval technique, and (d) their comparisons with in situ estimates. In panels (a)–(c), the dashed gray line shows the location of the aircraft, while the dotted line is a reference line to show 200 m above the aircraft's location. In panel d the retrieved rain rates were extrapolated to the aircraft level to compare with the in situ data. The gray line shows the rain rate retrieved with Z–R relationships, the orange line shows the rain rate retrieved with the ZV retrieval technique, and the blue line shows the rain rate retrieved with the radar-lidar retrieval technique. The black squares represent the rain rate estimated with in situ measurements, where rain rates are derived from averaged droplet size distribution (merged CDP and 2DS) over 20 s. Over that same time window, the median value of the retrieved rain rate time series was taken, denoted as gray dots (Z–R relationship), orange dots (ZV retrieval), and blue dots (radar-lidar retrieval).

extrapolated rain rate from the Z–R relationship (gray line), the extrapolated rain rate from ZV retrieval (orange line), and the extrapolated rain rate from radar-lidar retrieval (blue line). To further increase our confidence, we only compare the extrapolated rain rate from those periods where the original retrieved rain rate extends to within 200 m of the aircraft (i.e., when the rain extends down to dotted reference line). Another challenge is the limited sampling volume of the in situ probes. To overcome this difficulty, we average the in situ DSD over a 20s period when calculating the rain rate, marked as black squares in Figure 8d. We also calculate median of the corresponding retrievals over the same 20s time window, marked by the gray, orange and blue dots. It can be seen that the retrieved rain rate shows reasonable agreement with in situ data for this case.

KANG ET AL. 17 of 26

21698996, 2024, 6, Downloaded from https://agupubs.onlinelibrary.wiley.com/doi/10.1029/2023JD039831, Wiley Online Library on [26/03/2024]. See the Terms

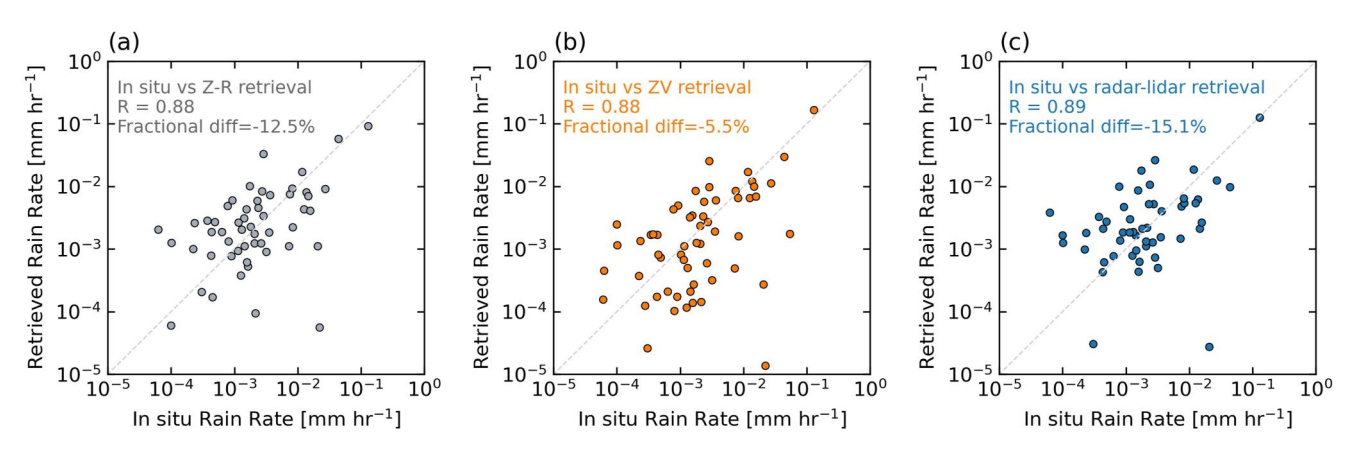


Figure 9. Comparison of in situ estimates with (a) Z–R retrieval, (b) ZV retrieval, and (c) radar-lidar retrieval for the entire campaign. The retrieved rain rates plotted here were extrapolated to the aircraft level (see Figure 8 and Figure S11 in Supporting Information S1) to compare with the in situ data. The fractional difference is calculated as the difference between the retrieved and in situ mean values divided by the average of the means.

We repeated this analysis for the liquid-precipitation retrievals for all the SOCRATES flights and summarized the results in Figure 9. Overall, the Z–R, ZV, and radar-lidar retrievals compare well with the in situ, with Pearson correlation coefficient of 0.88, 0.88 and 0.89, respectively. Despite the simplicity of the approach, even the rain rate derived from Z–R relationship shows skill in determining the rain rate as compared to the in situ values. The fractional difference in mean rain rate (difference in 20s mean/average of 20s mean) between the Z–R retrieval and in situ data is -12.5%. We can estimate the uncertainty in the retrieved rain rate via error propagation. If we estimated the uncertainty in reflectivity as 1.5 dB for reflectivity (following O'Connor et al., 2005) and 10% for lidar backscatter (e.g., Schwartz et al., 2019), we estimate the uncertainty in the radar-lidar retrieved rain rate would be 18%. Similarly, with an uncertainty of 1.5 dB for reflectivity, and 10% uncertainty for terminal fall velocity (see Tansey et al., 2022), we estimate the uncertainty in the ZV retrieved rain rate to be 44%. As for the Z–R relationship, using the uncertainties below-cloud sawtooth leg relationship from Table 2, the estimated uncertainty in rain rate is 42%. Relative to the expected uncertainties due simply to uncertainties in the inputs, all three retrievals compare well with the in situ data.

5. Vertical Distribution of Precipitation Properties

In this section, we will apply the precipitation observations and retrievals to study the vertical distribution of precipitation properties.

Figure 10 shows a violin plot of in situ measured precipitation properties at different altitudes and retrieved precipitation properties below the lidar-inferred cloud base. For each dataset, the white dot represents the median value, while the black bar represents the interquartile range. Perhaps surprisingly rain rate decreases going downward from the top half of the cloud (i.e., the largest rain rates are in the upper portion of the cloud). Medians of rain rate at the cloud top half, cloud bottom half, and below the cloud are $0.022~\text{mm hr}^{-1}$, $0.007~\text{mm hr}^{-1}$, and $0.001~\text{mm hr}^{-1}$. Similar to rain rate, there is also a decrease in precipitation number concentration (N_{precip}) and precipitation liquid water content (LWC_{precip}) moving downward from the top half of the cloud. In contrast, D_{precip} and σ_{precip} increase moving downward, that is bigger particles in the bottom half, and (just) below cloud. Overall, the retrieved precipitation properties (below the cloud base) compare well with the in situ estimates from the sawtooth below-cloud segments.

How do precipitation properties vary below cloud base? Figure 11 provides a more detailed view of the vertical distribution of precipitation properties below cloud base. Here, the column shows rain rate, N_{precip} , LWC_{precip} , D_{precip} , and σ_{precip} , respectively. The first two rows are histograms for radar-lidar and ZV retrievals, respectively. The last row is a box plot that summarizes both retrievals by binning the data vertically every 100 m. Here, we only consider data in those radar columns where rain extends at least 400 m below cloud base. Overall, both the rain rate and LWC_{precip} decrease exponentially with distance (as the change in the position of the distribution peak is roughly linear with distance on a log scale). Both retrievals have similar values and rates of decrease (panel (k) and panel (m)). The e-folding distance over which the rain rate decreases to 1/e (37%) of its initial value is about

KANG ET AL. 18 of 26

21698996, 2024, 6, Downloaded from https://agupubs.onlinelibrary.wiley.com/doi/10.1029/2023JD039831, Wiley Online Library on [26/03/2024]. See the Terms and Conditions (https://onlinelibrary.wiley.com/terms-and-conditions) on Wiley Online Library for rules of use; OA articles are governed by the applicable Creative Commons Licensea

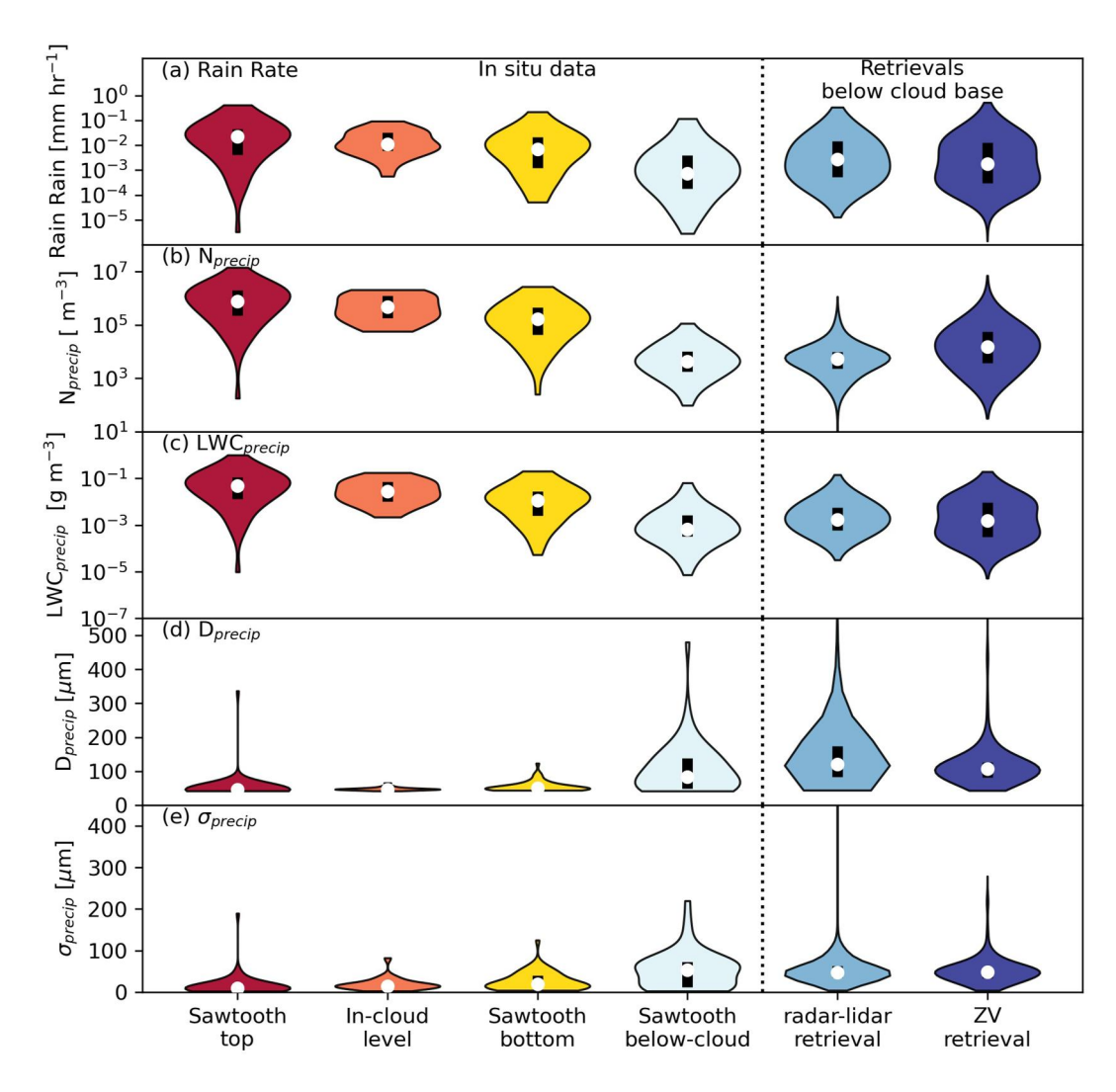


Figure 10. Violin plot for in situ measured precipitation properties at different altitudes and retrieved precipitation properties below cloud base: (a) rain rate (or precipitation liquid water flux), (b) precipitation number concentration N_{precip} , (c) precipitation liquid water content LWC $_{precip}$, (d) precipitation liquid water content weighted mean diameter D_{precip} , (e) precipitation liquid water content weighted width σ_{precip} . A violin plot can be regarded as a hybrid of a box plot and a kernel density plot. For each dataset, the white dot represents the median value, while the black bar represents the interquartile range, and the outer shape is the kernel density estimation to show the distribution of the data. In situ measured precipitation properties are from these legs (as marked in Figure S1 in Supporting Information S1): the top half of the cloud layer from sawtooth legs (sawtooth top); the bottom half of the cloud layer from sawtooth legs (sawtooth bottom); the below-cloud portion of the sawtooth legs (sawtooth below-cloud); and in-cloud level legs.

260 m for radar-lidar retrieval and 340 m for ZV retrieval. N_{precip} also decreases with distance, but we find the radar-lidar retrieval decreases more rapidly within 200 m below the cloud base, and the ZV retrieval shows higher N_{precip} than radar-lidar retrieval at different levels. This is consistent with (a result of) assuming a shape factor of zero in the ZV retrievals. The mean D_{precip} and σ_{precip} both increase with distance. Compared to radar-lidar retrieved D_{precip} , ZV retrieved D_{precip} is smaller overall (again consistent with the assumed shape factor), and has much less spread (variation) at any given altitude. Figure 10d shows that radar-lidar retrieved D_{precip} compares better with the in situ estimated D_{precip} from the below-cloud portion of the sawtooth legs than the ZV retrieved D_{precip} .

6. Rain Rate Dependence on Cloud Depth and Aerosol Concentration

In this section, we examine the degree to which precipitation can be diagnosed from cloud depth and cloud droplet or aerosol number concentration in the form (e.g., Comstock et al., 2004; Terai et al., 2012; Mann et al., 2014)

KANG ET AL. 19 of 26

21698996, 2024, 6, Downloaded from https://agupubs.onlinelibrary.wiley.com/doi/10.1029/2023JD039831, Wiley Online Library on [26/03/2024]. See the Terms and Conditions (https://onlinelibrary.wiley.com/terms-and-conditions) on Wiley Online Library for rules of use; OA articles are governed by the applicable Creative Commons License

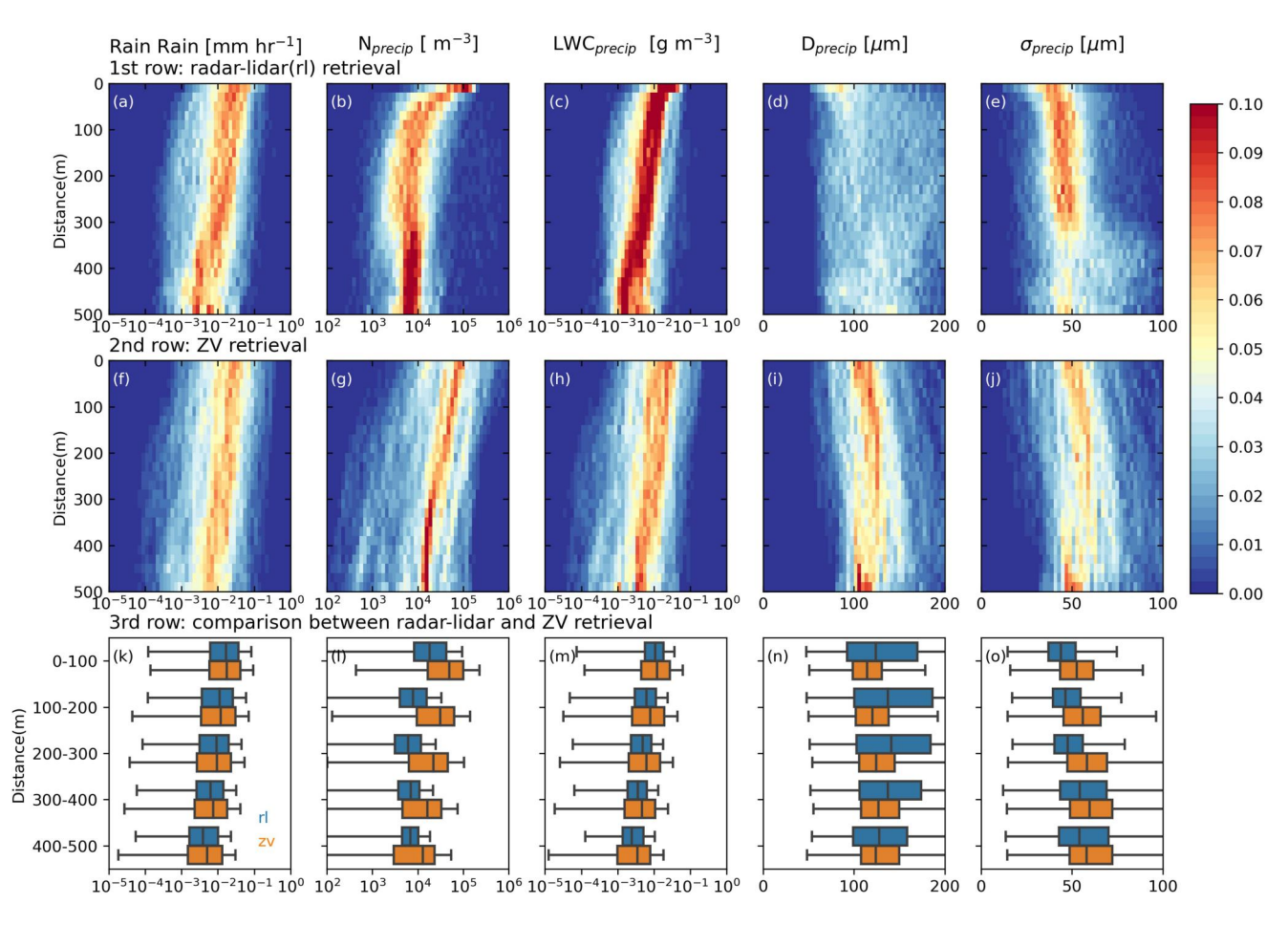


Figure 11. Vertical distributions of below-cloud-base liquid precipitation properties from retrievals (each column is rain rate, N_{precip} , LWC_{precip} , D_{precip} , σ_{precip} respectively). The first and second row is the histogram of retrieved precipitation properties below-cloud-base (data are normalized at each level), and y axis is the distance away from the cloud-base. The first row is the results from radar-lidar retrievals, the second row is the results from ZV retrievals. The last row is the box plot that summarizes the data in the first two rows by binning the data vertically every 100 m, where blue boxes are from radar-lidar retrievals, and orange boxes are from ZV retrievals.

$$R_{CR} = k H^{\alpha} N^{\beta} \tag{11}$$

where N is usually the cloud droplet (N_d) or aerosol number concentrations (N_a), H is cloud depth or liquid water path, and R_{CB} is rain rate at cloud base. To our knowledge, such a relationship has not been examined over the SO, except by Mace and Avey (2017) who used satellite retrievals. To examine this relationship over the SO, we focus on the below-cloud level legs (as marked in Figure S1 in Supporting Information S1) where variables can be obtained simultaneously and use the radar-lidar retrieved rain rate for R_{CB} , use the difference between cloud top and cloud base for H, and the accumulation mode aerosol concentrations with diameters larger than 70 nm from UHSAS for N_a . UHSAS essentially measures the dry particle size, as the collected aerosol particles were subjected to drying using a de-icing system, which modulates the temperature and pressure of the sampled air to prevent the formation of ice in the inlet (McCoy et al., 2021; Sanchez et al., 2021). To ensure that aerosol measurements from UHSAS were not contaminated by clouds or precipitation, we applied screening to the UHSAS data using both CDP and 2DS probes, following the method described by McCoy et al. (2021). We discarded data when the CDP liquid water content exceeded 0.01 g m⁻³ or the 2DS measured particle concentration exceeded 0.001 cm⁻³. Once these thresholds were exceeded, samples within the following 10 s were also removed as an extra precaution.

First, we broadly examine the rain rate dependence on either cloud depth or aerosol concentration, individually. Figure 12a shows a joint histogram of rain rate at cloud base and cloud depth. The histogram shows that rain rate

KANG ET AL. 20 of 26

21698996, 2024, 6, Downloaded from https://agupubs.onlinelibrary.wiley.com/doi/10.1029/2023JD039831, Wiley Online Library on [26/03/2024]. See the Terms and Conc

and-conditions) on Wiley Online Library for rules of use; OA articles are governed by the applicable Creative Commons Licensus

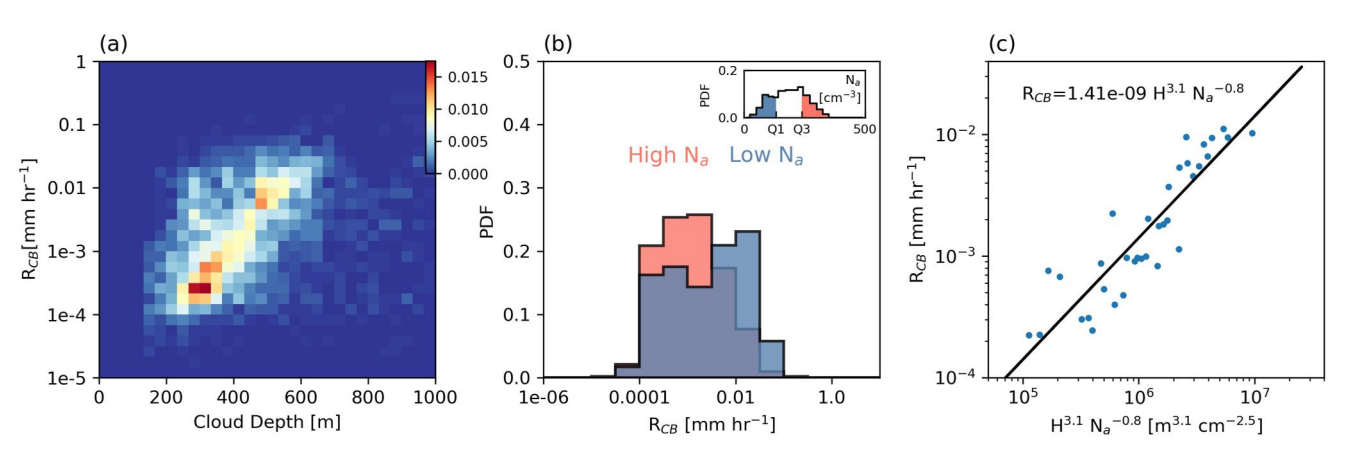


Figure 12. (a) Histogram of rain rate plotted as a function of cloud depth. (b) The probability density function of rain rate for conditions with low aerosol concentrations (lower than the first quartile, marked as blue) and high aerosol concentrations (higher than the third quartile, marked as red). (c) The rain rate at the cloud base is plotted as a function of the cloud depth, H, and aerosol concentration, N_a . Here H and N_a are the middle points for each cloud depth and aerosol concentration bin, while the rain rate at the cloud base is taken as the median value of rain rates in each cloud depth and aerosol concentration bin. The solid line shows the parametrization described in the main text

(at cloud base) scales with cloud depth, such that thicker clouds are associated with higher rain rates. This is consistent with previous studies (e.g., van Zanten et al., 2005; Pawlowska & Brenguier, 2003; Geoffroy et al., 2008). And to demonstrate the rain rate dependence on aerosol concentration, Figure 12b shows the probability density function of rain rate partitioned for conditions with low aerosol concentrations (lower than the first quartile, marked as blue) and high aerosol concentrations (higher than the third quartile, marked as red). Figure 12b shows that overall higher aerosol concentrations are associated with lower rain rates, consistent with aerosol suppression of precipitation.

How does rain rate relate to both cloud depth and aerosol concentration? To derive the coefficients in Equation 11, we divided cloud depth (H) up to 600 m into 6 bins, and divided aerosol concentrations (N_a) into 4 bins, and calculated the median rain rate for each H and N_a pair. Then we performed a linear least squares regression on the natural logarithms of data from these 24 bins (Figure 12c). The derived relationship is $R_{CB} = 1.41 \times 10^{-9} \ H^{3.1} \ N_a^{-0.8}$, with H in m, N_a in cm⁻³, and R_{CB} in mm hr⁻¹. Using a bootstrap resampling technique, we estimate that the one-sigma uncertainty range for the exponent α (for H) ranges from 2.8 to 3.4, while the range for exponent β (for N_a)ranges from -1.0 to -0.7. The relationship we derive here is broadly similar to previous studies for stratocumulus in other regions. Specifically, the exponent α for cloud depth typically is about 3 (van Zanten et al., 2005; Pawlowska & Brenguier, 2003; Lu et al., 2009), and the exponent β for number concentration (cloud droplet concentration or cloud condensation nuclei) typically ranges between -1.75 and -0.66 (van Zanten et al., 2005; Mann et al., 2014; Lu et al., 2009; Comstock et al., 2004). The exponent β of -0.8 for aerosol concentration we derived here is smaller than exponent β of -0.32 in Mace and Avey (2017, hereafter M17), estimated using satellite-estimated cloud droplet number concentration, liquid water path, and rain rate for the SO. We will discuss this difference further in the next section.

7. Conclusions

In this study, we examine in-and-below-cloud precipitation properties for stratocumulus over the Southern Ocean (SO), using data collected from airborne W-band Cloud Radar (HCR), High Spectral Resolution Lidar (HSRL), and various in situ probes during the Southern Ocean Clouds Radiation Aerosol Transport Experimental Study (SOCRATES) in January–February 2018.

Overall, we find that about 60% of the stratocumulus were precipitating, and about 80% of the stratocumulus were cold-topped (with a cloud top temperature $<0^{\circ}$ C) based on periods where the aircraft were flying below cloud and the radar and lidar pointing toward the zenith. We determine the precipitation phase using the lidar particle linear depolarization ratio PLDR and find that about 60% of the precipitation is liquid phase, and about 20% of the precipitation is ice phase, with the remaining 20% being ambiguous. While we cannot rule out the possibility that any individual ambiguous case is pure liquid, most of such cases are likely to have ice or mixed-phase

KANG ET AL. 21 of 26

21698996, 2024, 6, Downloaded from https://agupubs.onlinelibrary.wiley.com/doi/10.1029/2023JD039831, Wiley Online Library on [26/03/2024]. See the Terms and Conditions

onditions) on Wiley Online Library for rules of use; OA articles are governed by the applicable Creative Commons Licenso

precipitation present. Further, for cold-topped clouds, we find that when the reflectivity factor is less than about -10 dBZ, the precipitation is predominantly liquid, while for reflectivity factors greater than 0 dBZ, precipitation is predominantly ice. These results are similar to what was found by Mace and Protat (2018) based on CAPRICORN data during March–April 2016, as well as a recent study by Tansey et al. (2023) based on surface data collected at Macquarie Island (54.5°S) between March and November 2016. The SOCRATES data, collected in the Southern Hemisphere Summer, in January and February 2018, suggests this relationship is likely characteristic of SO low clouds throughout the year, and suggests that the measured reflectivity factor might be used as a proxy to determine the precipitation phase for *cold-topped Southern Ocean stratocumulus* with CloudSat (or other "radar only") retrievals where no other information is available to constrain the precipitation phase.

For liquid-phase precipitation, we performed retrievals for precipitation rain rate and other microphysical parameters based on radar and lidar, with the goal to test a hierarchy of retrieval methods, from the simplest Z–R relationship approach where only radar reflectivity (Z) is used to estimate the rain rate, to a reflectivity-velocity (ZV) retrieval where there are two observables (inputs to the retrieval), to a radar-lidar retrieval with three observables. Our evaluation shows that rain rates from the Z–R, ZV, and radar-lidar retrievals all compare well with the in situ rain rates, with Pearson correlation coefficient of 0.88. 0.88 and. 0.89, and fractional difference (difference between the retrieved and in situ mean value divided by the average of the means) of only -12.5%, -5.5%, and -15.1%, respectively. In addition to rain rate, ZV, and radar-lidar retrievals can retrieve other precipitation properties, such as precipitation number concentration, precipitation liquid water content, number concentration, size, and width. The overall statistics and distribution of these retrieved precipitation properties below the cloud base, also compare well with in situ estimates from the sawtooth below-cloud segments. This good performance gives us some confidence in using these retrieval techniques for SO stratocumulus, including in our recently published manuscript that examines coalescence scavenging in SO stratocumulus (Kang et al., 2022).

Despite the good retrieval performance overall, there are important caveats. When developing the power-law relationships between reflectivity (Z) and rain rate (R) following $Z = aR^b$ we found the b exponent varied little with altitude and had a value around 1.2 to 1.4. This is similar to values obtained in previous studies for stratocumulus in other regions (Comstock et al., 2004; van Zanten et al., 2005). The a coefficient, on the other hand, increases as one moves from the cloud layer to the surface. In general, one can derive a power-law relationship between Z and R based on the assumption of a modified gamma distribution (e.g., Rosenfeld & Ulbrich, 2003), and doing so shows that one should expect the a coefficient to depend on the total droplet number concentration. Given the vertical variations in the precipitation droplet number concentration (see Figures 10 and 11), the vertical variation in the a coefficient is not surprising. But such also hints that the a coefficient may well vary with the accumulation mode aerosol concentration or other factors that control the cloud droplet number concentration. So Z-R relationships should be used with some caution in studies intending to establish relationships between rain rates and aerosols. We also find that the derived Z-R relationships are sensitive to whether ones exclude drops with diameters smaller than 40 µm when in cloud, because these drops make a nontrivial contribution to total liquid water flux, as perhaps first noted by Nicholls (1984). Our analysis suggests that below-cloud Z-R equations should be applied with caution to in-cloud reflectivity measurements, and should be expected to underestimate the total liquid water flux in cloud.

Comparing the ZV retrieval with radar-lidar retrieval shows that both retrievals capture the mean vertical structure of precipitation microphysics below cloud. Based on in situ data and retrievals, we found that rain rate, precipitation number concentration (N_{precip}), precipitation liquid water (LWC_{precip}) all decrease as one gets closer to the surface, while precipitation liquid water content weighted mean diameter (D_{precip}) and width (σ_{precip}) increases. The e-folding distance over which the rain rate decreases to 1/e (37%) of its initial value is about 260 m for radar-lidar retrieval and 340 m for ZV retrieval. However, we find that both D_0 and N_{precip} from the ZV retrieval have less spatial variability than that from the radar-lidar retrieval, and assuming a shape factor of $\mu=0$, results in the ZV retrieved mean D_0 being a bit too small and N_{precip} being too large as compared to the radar-lidar retrieval. This is because the shape factor is not constant and in particular, because the shape factor in the stronger precipitation shafts below the thicker portion of the clouds should be larger than zero (because the precipitation DSD is narrower with a more well-defined peaked rather than a broad exponential-like distribution).

This study also explored rain rate dependence on cloud depth and aerosol concentration. Rain rate at cloud base (R_{CB}) increases with cloud depth (H) and decreases with aerosol concentration (N_a) . Using a least squares regression, we found R_{CB} varies with $H^{3.1}$ $N_a^{-0.8}$, which is broadly consistent with estimates for stratocumulus in

KANG ET AL. 22 of 26

21698996, 2024, 6, Downloaded from https://agupubs.onlinelibarry.wiley.com/doi/10.1029/2023JD039831, Wiley Online Library on [26/03/2024]. See the Terms and Conditions (https://agupubs.on/doi/10.1029/2023JD039831, Wiley Online Library on [26/03/2024].

and-conditions) on Wiley Online Library for rules of use; OA articles

previous studies over other regions (van Zanten et al., 2005; Pawlowska & Brenguier, 2003; Lu et al., 2009; Mann et al., 2014; Comstock et al., 2004). However as noted in Section 6, our results differ from the satellite-based estimates for the SO by Mace and Avey (2017), hereafter M17, who suggest an exponent of -0.32 for the aerosol concentration based on satellite retrievals. M17 also noted that their estimates differ from previous studies in other regions. There are a variety of potential reasons for the different results in our study and in M17. The first obvious reason is different data sources. Our study used in situ measured N_a and retrieved rain rate with airborne radar and lidar measurements, while M17 used N_d , liquid water path, and rain rate derived from MODIS and Cloudsat based on an optimal estimation algorithm. Another reason might be different cloud populations; where in our study about 80% of the clouds are cold-topped, M17 restricted their analysis to warm-topped clouds. Data collected during the Macquarie Island Cloud and Radiation Experiment (MICRE), suggest that warm-topped SO clouds are geometrically thinner and closer to the surface than cold-topped clouds (Tansey et al., 2023). As-is, we end this study here, leaving a regime-dependent analysis of precipitation susceptibility for a future study. As more data are collected, including in future campaigns such as the upcoming Clouds And Precipitation Experiment at Kennaook (CAPE-K) that will begin in March 2024, the aerosol sensitivity of low altitude SO clouds are certain to be the focus of future multi- or cross-experiments studies.

Data Availability Statement

The authors would like to acknowledge the SOCRATES Project for providing data through the SOCRATES Data Archive Center (SDAC) at NCAR's Earth Observing Laboratory (EOL). The dataset derived based on this manuscript is available at EOL Data Archive as SOCRATES Liquid Precipitation Properties Retrieval Product (Kang et al., 2024). Other data used in this manuscript can also be accessed via EOL Data Archive: (a) low rate (1 Hz) navigation, state parameter, and microphysics flight-level data version 1.4 that contain data from many probes, including CDP and UHSAS (UCAR/NCAR - Earth Observing Laboratory, 2022); (b) 2DS data version 1.1 (Wu & McFarquhar, 2019); (c) SOCRATES Cloud Phase Product version 1.0 (D'Alessandro et al., 2022); (d) HCR radar and HSRL lidar moments 2 Hz data version 3.1 (NCAR/EOL HCR Team & NCAR/EOL HSRL Team, 2022). Miepython is developed by Prahl (2023).

Acknowledgments References

This work was supported by the U.S.

National Science Foundation on grant

contribution from the many individuals

Science and Aircraft Instrument Teams.

helping with radar data processing. We

would like to thank open-source codes

such as miepython and CloudnetPy. We

appreciate the reviewers for their time and

effort in reviewing this manuscript. Their

valuable comments have helped us

improve the quality of this work.

We thank Dr. Ulrike Romatschke for

Observing Laboratory, SOCRATES

AGS-2124993. We would like to thank the

and teams associated with the NCAR Earth

Beard, K. V. (1976). Terminal velocity and shape of cloud and precipitation drops Aloft. *Journal of the Atmospheric Sciences*, *33*(5), 851–864. https://doi.org/10.1175/1520-0469(1976)033<0851:TVASOC>2.0.CO;2
Bellouin, N., Quaas, J., Gryspeerdt, E., Kinne, S., Stier, P., Watson-Parris, D., et al. (2020). Bounding global aerosol radiative forcing of climate

Bellouin, N., Quaas, J., Gryspeerdt, E., Kinne, S., Stier, P., Watson-Parris, D., et al. (2020). Bounding global aerosol radiative forcing of climate change. *Reviews of Geophysics*, 58(1), e2019RG000660. https://doi.org/10.1029/2019RG000660

Bjordal, J., Storelvmo, T., Alterskjær, K., & Carlsen, T. (2020). Equilibrium climate sensitivity above 5°C plausible due to state-dependent cloud feedback. Nature Geoscience, 13(11), 718–721. https://doi.org/10.1038/s41561-020-00649-1

Bodas-Salcedo, A., Hill, P. G., Furtado, K., Williams, K. D., Field, P. R., Manners, J. C., et al. (2016). Large contribution of supercooled liquid clouds to the solar radiation budget of the Southern Ocean. *Journal of Climate*, 29(11), 4213–4228. https://doi.org/10.1175/JCLI-D-15-0564.1 Bohren, C. F., & Huffman, D. R. (1983). *Absorption and scattering of light by small particles*. Wiley Online Library.

Cesana, G. V., Khadir, T., Chepfer, H., & Chiriaco, M. (2022). Southern Ocean solar reflection biases in CMIP6 models linked to cloud phase and vertical structure representations. *Geophysical Research Letters*, 49(22), e2022GL099777. https://doi.org/10.1029/2022GL099777

Comstock, K. K., Wood, R., Yuter, S. E., & Bretherton, C. S. (2004). Reflectivity and rain rate in and below drizzling stratocumulus. Quarterly Journal of the Royal Meteorological Society, 130(603), 2891–2918. https://doi.org/10.1256/qj.03.187

D'Alessandro, J., Schima, J., & McFarquhar, G. (2022). SOCRATES Cloud Phase Product. Version 1.0 [Dataset]. UCAR/NCAR - Earth Observing Laboratory. https://doi.org/10.26023/S6WS-G5QE-H113

D'Alessandro, J. J., McFarquhar, G. M., Wu, W., Stith, J. L., Jensen, J. B., & Rauber, R. M. (2021). Characterizing the occurrence and spatial heterogeneity of liquid, ice, and mixed phase low-level clouds over the Southern Ocean using in situ observations acquired during SOCRATES. *Journal of Geophysical Research: Atmospheres*, 126(11), e2020JD034482. https://doi.org/10.1029/2020JD034482

DMT. (2013). Ultra high sensitivity aerosol spectrometer (UHSAS) Operator Manual.

Eastman, R., Lebsock, M., & Wood, R. (2019). Warm rain rates from AMSR-E 89-GHz brightness temperatures trained using CloudSat rain-rate observations. *Journal of Atmospheric and Oceanic Technology*, 36(6), 1033–1051. https://doi.org/10.1175/JTECH-D-18-0185.1

Ellis, S. M., Tsai, P., Burghart, C., Romatschke, U., Dixon, M., Vivekanandan, J., et al. (2019). Use of the earth's surface as a reference to correct airborne nadir-looking radar radial velocity measurements for platform motion. *Journal of Atmospheric and Oceanic Technology*, 36(7), 1343–1360. https://doi.org/10.1175/JTECH-D-19-0019.1

Ellis, T. D., L'Ecuyer, T., Haynes, J. M., & Stephens, G. L. (2009). How often does it rain over the global oceans? The perspective from CloudSat. Geophysical Research Letters, 36(3). https://doi.org/10.1029/2008GL036728

Eloranta, E. E. (2005). High spectral resolution lidar. In C. Weitkamp (Ed.), Lidar: Range-Resolved optical remote sensing of the atmosphere (pp. 143–163). Springer. https://doi.org/10.1007/0-387-25101-4_5

Faber, S., French, J. R., & Jackson, R. (2018). Laboratory and in-flight evaluation of measurement uncertainties from a commercial Cloud Droplet Probe (CDP). Atmospheric Measurement Techniques, 11(6), 3645–3659. https://doi.org/10.5194/amt-11-3645-2018

Frisch, A. S., Fairall, C. W., & Snider, J. B. (1995). Measurement of stratus cloud and drizzle parameters in ASTEX with a kα-band Doppler radar and a microwave radiometer. *Journal of the Atmospheric Sciences*, 52(16), 2788–2799. https://doi.org/10.1175/1520-0469(1995)052<2788: MOSCAD>2.0.CO;2

KANG ET AL. 23 of 26

- Frölicher, T. L., Sarmiento, J. L., Paynter, D. J., Dunne, J. P., Krasting, J. P., & Winton, M. (2015). Dominance of the Southern Ocean in anthropogenic carbon and heat uptake in CMIP5 models. *Journal of Climate*, 28(2), 862–886. https://doi.org/10.1175/JCLI-D-14-00117.1
- Geoffroy, O., Brenguier, J.-L., & Sandu, I. (2008). Relationship between drizzle rate, liquid water path and droplet concentration at the scale of a stratocumulus cloud system. Atmospheric Chemistry and Physics, 8(16), 4641–4654. https://doi.org/10.5194/acp-8-4641-2008
- Ghate, V. P., & Cadeddu, M. P. (2019). Drizzle and turbulence below closed cellular marine stratocumulus clouds. *Journal of Geophysical Research-Atmospheres*, 124(11), 2018JD030141. https://doi.org/10.1029/2018JD030141
- Grecu, M., Olson, W. S., Munchak, S. J., Ringerud, S., Liao, L., Haddad, Z., et al. (2016). The GPM combined algorithm. *Journal of Atmospheric and Oceanic Technology*, 33(10), 2225–2245. https://doi.org/10.1175/JTECH-D-16-0019.1
- Hamilton, D. S., Lee, L. A., Pringle, K. J., Reddington, C. L., Spracklen, D. V., & Carslaw, K. S. (2014). Occurrence of pristine aerosol environments on a polluted planet. *Proceedings of the National Academy of Sciences*, 111(52), 18466–18471. https://doi.org/10.1073/pnas.
- Haynes, J. M., L'Ecuyer, T. S., Stephens, G. L., Miller, S. D., Mitrescu, C., Wood, N. B., & Tanelli, S. (2009). Rainfall retrieval over the ocean with spaceborne W-band radar. *Journal of Geophysical Research: Atmospheres*, 114(D8). https://doi.org/10.1029/2008JD009973
- Illingworth, A. J., & Blackman, T. M. (2002). The need to represent raindrop size spectra as normalized gamma distributions for the interpretation of polarization radar observations. *Journal of Applied Meteorology*, 41(3), 286–297. https://doi.org/10.1175/1520-0450(2002)041<0286: TNTRRS>2.0.CO;2
- Kang, L., Marchand, R., & Smith, W. (2021). Evaluation of MODIS and Himawari-8 low clouds retrievals over the Southern Ocean with in situ measurements from the SOCRATES campaign. Earth and Space Science, 8(3), e2020EA001397. https://doi.org/10.1029/2020EA001397
- Kang, L., Marchand, R., & Wood, R. (2024). SOCRATES: Liquid precipitation properties retrieval product. Version 1.0. [Dataset]. UCAR/NCAR Earth Observing Laboratory. https://doi.org/10.26023/XTCR-ZDTN-Q0K
- Kang, L., Marchand, R. T., Wood, R., & McCoy, I. L. (2022). Coalescence scavenging drives droplet number concentration in Southern Ocean low clouds. Geophysical Research Letters, 49(7), e2022GL097819. https://doi.org/10.1029/2022GL097819
- Khatiwala, S., Primeau, F., & Hall, T. (2009). Reconstruction of the history of anthropogenic CO2 concentrations in the ocean. *Nature*, 462(7271), 346–349. https://doi.org/10.1038/nature08526
- Klepp, C., Michel, S., Protat, A., Burdanowitz, J., Albern, N., Kähnert, M., et al. (2018). OceanRAIN, a new in-situ shipboard global ocean surface-reference dataset of all water cycle components. Scientific Data, 5(1), 180122. https://doi.org/10.1038/sdata.2018.122
- Lance, S., Brock, C. A., Rogers, D., & Gordon, J. A. (2010). Water droplet calibration of the Cloud Droplet Probe (CDP) and in-flight performance in liquid, ice and mixed-phase clouds during ARCPAC. *Atmospheric Measurement Techniques*, *3*(6), 1683–1706. https://doi.org/10.5194/amt-
- Lee, L. A., Reddington, C. L., & Carslaw, K. S. (2016). On the relationship between aerosol model uncertainty and radiative forcing uncertainty.

 Proceedings of the National Academy of Sciences, 113(21), 5820–5827. https://doi.org/10.1073/pnas.1507050113
- Lu, M.-L., Sorooshian, A., Jonsson, H. H., Feingold, G., Flagan, R. C., & Seinfeld, J. H. (2009). Marine stratocumulus aerosol-cloud relationships in the MASE-II experiment: Precipitation susceptibility in eastern Pacific marine stratocumulus. *Journal of Geophysical Research: Atmo-spheres*, 114(D24). https://doi.org/10.1029/2009JD012774
- Mace, G. G., & Avey, S. (2017). Seasonal variability of warm boundary layer cloud and precipitation properties in the Southern Ocean as diagnosed from A-Train data. *Journal of Geophysical Research: Atmospheres*, 122(2), 1015–1032. https://doi.org/10.1002/2016JD025348
- Mace, G. G., Benson, S., & Hu, Y. (2020). On the frequency of occurrence of the ice phase in supercooled Southern Ocean low clouds derived from CALIPSO and CloudSat. Geophysical Research Letters, 47(14), e2020GL087554. https://doi.org/10.1029/2020GL087554
- Mace, G. G., Heymsfield, A. J., & Poellot, M. R. (2002). On retrieving the microphysical properties of cirrus clouds using the moments of the millimeter-wavelength Doppler spectrum. *Journal of Geophysical Research*, 107(D24). AAC 22-1-AAC 22-26. https://doi.org/10.1029/ 2001JD001308
- Mace, G. G., & Protat, A. (2018). Clouds over the Southern Ocean as observed from the R/V investigator during CAPRICORN. Part I: Cloud occurrence and phase partitioning. *Journal of Applied Meteorology and Climatology*, 57(8), 1783–1803. https://doi.org/10.1175/JAMC-D-17-0194.1
- Mann, J. A. L., Christine Chiu, J., Hogan, R. J., O'Connor, E. J., L'Ecuyer, T. S., Stein, T. H. M., & Jefferson, A. (2014). Aerosol impacts on drizzle properties in warm clouds from ARM Mobile Facility maritime and continental deployments. *Journal of Geophysical Research: At-mospheres*, 119(7), 4136–4148. https://doi.org/10.1002/2013JD021339
- Marchand, R., Mace, G. G., Ackerman, T., & Stephens, G. (2008). Hydrometeor detection using Cloudsat—An Earth-Orbiting 94-GHz cloud radar. *Journal of Atmospheric and Oceanic Technology*, 25(4), 519–533. https://doi.org/10.1175/2007JTECHA1006.1
- Marchand, R. T., Ackerman, T. P., & Moroney, C. (2007). An assessment of Multiangle Imaging Spectroradiometer (MISR) stereo-derived cloud top heights and cloud top winds using ground-based radar, lidar, and microwave radiometers. *Journal of Geophysical Research: Atmospheres*, 112(D6), https://doi.org/10.1029/2006JD007091
- McCoy, I. L., Bretherton, C. S., Wood, R., Twohy, C. H., Gettelman, A., Bardeen, C. G., & Toohey, D. W. (2021). Influences of recent particle formation on Southern Ocean aerosol variability and low cloud properties. *Journal of Geophysical Research: Atmospheres*, 126(8), e2020JD033529. https://doi.org/10.1029/2020JD033529
- McCoy, I. L., McCoy, D. T., Wood, R., Regayre, L., Watson-Parris, D., Grosvenor, D. P., et al. (2020). The hemispheric contrast in cloud microphysical properties constrains aerosol forcing. Proceedings of the National Academy of Sciences of the United States of America, 117(32), 18998–19006. https://doi.org/10.1073/pnas.1922502117
- McFarquhar, G. M., Bretherton, C. S., Marchand, R., Protat, A., DeMott, P. J., Alexander, S. P., et al. (2021). Observations of clouds, aerosols, precipitation, and surface radiation over the Southern Ocean: An overview of CAPRICORN, MARCUS, MICRE, and SOCRATES. *Bulletin of the American Meteorological Society*, 102(4), E894–E928. https://doi.org/10.1175/BAMS-D-20-0132.1
- McFarquhar, G. M., Finlon, J. A., Stechman, D. M., Wu, W., Jackson, R. C., & Freer, M. (2018). University of Illinois/Oklahoma optical Array probe (OAP) processing software [Software]. Zenodo. https://doi.org/10.5281/zenodo.1285969
- Mitrescu, C., L'Ecuyer, T., Haynes, J., Miller, S., & Turk, J. (2010). CloudSat precipitation profiling algorithm—Model description. *Journal of Applied Meteorology and Climatology*, 49(5), 991–1003. https://doi.org/10.1175/2009JAMC2181.1
- Montoya Duque, E., Huang, Y., Siems, S. T., May, P. T., Protat, A., & McFarquhar, G. M. (2022). A characterization of clouds and precipitation over the Southern Ocean from synoptic to micro scales during the CAPRICORN field campaigns. *Journal of Geophysical Research: Atmospheres*, 127(17), e2022JD036796. https://doi.org/10.1029/2022JD036796
- Mülmenstädt, J., Salzmann, M., Kay, J. E., Zelinka, M. D., Ma, P.-L., Nam, C., et al. (2021). An underestimated negative cloud feedback from cloud lifetime changes. *Nature Climate Change*, 11(6), 508–513. https://doi.org/10.1038/s41558-021-01038-1
- NCAR/EOL HCR Team & NCAR/EOL HSRL Team. (2022). SOCRATES: NCAR HCR radar and HSRL lidar moments data. Version 3.1 [Dataset]. UCAR/NCAR Earth Observing Laboratory. https://doi.org/10.5065/D64J0CZS

KANG ET AL. 24 of 26

21698996, 2024, 6, Downloaded from

onlinelibrary.wiley.com/doi/10.1029/2023JD039831, Wiley Online Library.

on [26/03/2024]. See the Terms

- Nicholls, S. (1984). The dynamics of stratocumulus: Aircraft observations and comparisons with a mixed layer model. *Quarterly Journal of the Royal Meteorological Society*, 110(466), 783–820. https://doi.org/10.1002/qj.49711046603
- O'Connor, E. J., Hogan, R. J., & Illingworth, A. J. (2005). Retrieving stratocumulus drizzle parameters using Doppler radar and lidar. *Journal of Applied Meteorology and Climatology*, 44(1), 14–27. https://doi.org/10.1175/JAM-2181.1
- Orr, B. W., & Kropfli, R. A. (1999). A method for estimating particle fall velocities from vertically pointing Doppler radar. *Journal of Atmospheric and Oceanic Technology*, 16(1), 29–37. https://doi.org/10.1175/1520-0426(1999)016<0029:AMFEPF>2.0.CO;2
- O'Shea, S. J., Choularton, T. W., Lloyd, G., Crosier, J., Bower, K. N., Gallagher, M., et al. (2016). Airborne observations of the microphysical structure of two contrasting cirrus clouds. *Journal of Geophysical Research: Atmospheres*, 121(22), 13510–13536. https://doi.org/10.1002/2016ID025278
- Pawlowska, H., & Brenguier, J.-L. (2003). An observational study of drizzle formation in stratocumulus clouds for general circulation model (GCM) parameterizations. *Journal of Geophysical Research: Atmospheres*, 108(D15). https://doi.org/10.1029/2002JD002679
- Petty, G. W., & Huang, W. (2011). The modified gamma size distribution applied to inhomogeneous and nonspherical particles: Key relationships and conversions. *Journal of the Atmospheric Sciences*, 68(7), 1460–1473. https://doi.org/10.1175/2011JAS3645.1
- Prahl, S. (2023). miepython: Pure python implementation of Mie scattering [Software]. Zenodo. https://zenodo.org/records/8218010
- Protat, A., Klepp, C., Louf, V., Petersen, W. A., Alexander, S. P., Barros, A., et al. (2019). The latitudinal variability of oceanic rainfall properties and its implication for satellite retrievals: 1. Drop size distribution properties. *Journal of Geophysical Research: Atmospheres*, 124(23), 13291–13311. https://doi.org/10.1029/2019JD031010
- Romatschke, U., Dixon, M., Tsai, P., Loew, E., Vivekanandan, J., Emmett, J., & Rilling, R. (2021). The NCAR airborne 94-GHz cloud radar: Calibration and data processing. *Data*, 6(6), 66. https://doi.org/10.3390/data6060066
- Rosenfeld, D., & Ulbrich, C. W. (2003). Cloud microphysical properties, processes, and rainfall estimation opportunities. *Meteorological Monographs*, 30(52), 237–258. https://doi.org/10.1175/0065-9401(2003)030<0237:CMPPAR>2.0.CO;2
- Sanchez, K. J., Roberts, G. C., Saliba, G., Russell, L. M., Twohy, C., Reeves, J. M., et al. (2021). Measurement report: Cloud processes and the transport of biological emissions affect southern ocean particle and cloud condensation nuclei concentrations. Atmospheric Chemistry and Physics, 21(5), 3427–3446. https://doi.org/10.5194/acp-21-3427-2021
- Sarkar, M., Zuidema, P., & Ghate, V. (2021). Clarifying remotely retrieved precipitation of shallow marine clouds from the NSF/NCAR Gulfstream V. Journal of Atmospheric and Oceanic Technology, 38(9), 1657–1670. https://doi.org/10.1175/JTECH-D-20-0166.1
- Schima, J., McFarquhar, G., Romatschke, U., Vivekanandan, J., D'Alessandro, J., Haggerty, J., et al. (2022). Characterization of Southern Ocean boundary layer clouds using airborne radar, lidar, and in situ cloud data: Results from SOCRATES. *Journal of Geophysical Research: At-mospheres*, 127(21), e2022JD037277. https://doi.org/10.1029/2022JD037277
- Schwartz, M. C., Ghate, V. P., Albrecht, B. A., Zuidema, P., Cadeddu, M. P., Vivekanandan, J., et al. (2019). Merged cloud and precipitation dataset from the HIAPER GV for the Cloud System Evolution in the Trades (CSET) campaign. *Journal of Atmospheric and Oceanic Tech*nology, 36(6), 921–940. https://doi.org/10.1175/JTECH-D-18-0111.1
- Seto, S., Iguchi, T., & Oki, T. (2013). The basic performance of a precipitation retrieval algorithm for the global precipitation measurement mission's single/dual-frequency radar measurements. *IEEE Transactions on Geoscience and Remote Sensing*, 51(12), 5239–5251. https://doi.org/10.1109/TGRS.2012.2231686
- Smalley, K. M., Lebsock, M. D., Eastman, R., Smalley, M., & Witte, M. K. (2022). A Lagrangian analysis of pockets of open cells over the southeastern Pacific. Atmospheric Chemistry and Physics, 22(12), 8197–8219. https://doi.org/10.5194/acp-22-8197-2022
- Tan, I., Storelvmo, T., & Zelinka, M. D. (2016). Observational constraints on mixed-phase clouds imply higher climate sensitivity. Science, 352(6282), 224–227. https://doi.org/10.1126/science.aad5300
- Tansey, E., Marchand, R., Alexander, S. P., Klekociuk, A. R., & Protat, A. (2023). Southern Ocean low cloud and precipitation phase observed during the Macquarie Island Cloud and Radiation Experiment (MICRE). *Journal of Geophysical Research: Atmospheres*, 128(17). e2023JD039205. https://doi.org/10.1029/2023JD039205
- Tansey, E., Marchand, R., Protat, A., Alexander, S. P., & Ding, S. (2022). Southern Ocean precipitation characteristics observed from CloudSat and ground instrumentation during the Macquarie Island Cloud & Radiation Experiment (MICRE): April 2016 to March 2017. *Journal of Geophysical Research: Atmospheres*, 127(5), e2021JD035370. https://doi.org/10.1029/2021JD035370
- Terai, C. R., Wood, R., Leon, D. C., & Zuidema, P. (2012). Does precipitation susceptibility vary with increasing cloud thickness in marine stratocumulus? Atmospheric Chemistry and Physics, 12(10), 4567–4583. https://doi.org/10.5194/acp-12-4567-2012
- Trenberth, K. E., & Fasullo, J. T. (2010). Simulation of present-day and twenty-first-century energy budgets of the southern oceans. *Journal of Climate*, 23(2), 440–454. https://doi.org/10.1175/2009JCLI3152.1
- UCAR/NCAR-Earth Observing Laboratory. (2022). SOCRATES: Low Rate (LRT 1 sps) navigation, state parameter, and microphysics flight-level data. Version 1.4 [Dataset]. UCAR/NCAR Earth Observing Laboratory. https://doi.org/10.5065/D6M32TM9
- Ulbrich, C. W. (1983). Natural variations in the analytical form of the raindrop size distribution. *Journal of Applied Meteorology and Climatology*, 22(10), 1764–1775. https://doi.org/10.1175/1520-0450(1983)022<1764:NVITAF>2.0.CO;2
- van Zanten, M. C., Stevens, B., Vali, G., & Lenschow, D. H. (2005). Observations of drizzle in nocturnal marine stratocumulus. *Journal of the Atmospheric Sciences*, 62(1), 88–106. https://doi.org/10.1175/JAS-3355.1
- Vivekanandan, J., Ellis, S., Tsai, P., Loew, E., Lee, W.-C., Emmett, J., et al. (2015). A wing pod-based millimeter wavelength airborne cloud radar. Geoscientific Instrumentation, Methods and Data Systems, 4(2), 161–176. https://doi.org/10.5194/gi-4-161-2015
- Wang, H., & Feingold, G. (2009). Modeling mesoscale cellular structures and drizzle in marine stratocumulus. Part I: Impact of drizzle on the formation and evolution of open cells. *Journal of the Atmospheric Sciences*, 66(11), 3237–3256. https://doi.org/10.1175/2009JAS3022.1
- Wang, Y., McFarquhar, G. M., Rauber, R. M., Zhao, C., Wu, W., Finlon, J. A., et al. (2020). Microphysical properties of generating cells over the Southern Ocean: Results from SOCRATES. *Journal of Geophysical Research: Atmospheres*, 125(13), e2019JD032237. https://doi.org/10. 1029/2019JD032237
- Wilks, D. S. (1997). Resampling hypothesis tests for autocorrelated fields. *Journal of Climate*, 10(1), 65–82. https://doi.org/10.1175/1520-0442 (1997)010<0065:RHTFAF>2.0.CO;2
- Wiscombe, J. (1979). Mie scattering calculations: Advances in technique and fast, vector-speed computer codes. https://doi.org/10.5065/ D67P4414
- Wood, R. (2005). Drizzle in stratiform boundary layer clouds. Part II: Microphysical aspects. Journal of the Atmospheric Sciences, 62(9), 3034–3050. https://doi.org/10.1175/JAS3530.1
- Wood, R. (2012). Stratocumulus clouds. Monthly Weather Review, 140(8), 2373–2423. https://doi.org/10.1175/MWR-D-11-00121.1
- Wood, R., Bretherton, C. S., Leon, D., Clarke, A. D., Zuidema, P., Allen, G., & Coe, H. (2011). An aircraft case study of the spatial transition from closed to open mesoscale cellular convection over the Southeast Pacific. Atmospheric Chemistry and Physics, 11(5), 2341–2370. https://doi.org/10.5194/acp-11-2341-2011

KANG ET AL. 25 of 26



Journal of Geophysical Research: Atmospheres

- 10.1029/2023JD039831
- Wu, W., & McFarquhar, G. (2019). NSF/NCAR GV HIAPER 2D-S Particle Size Distribution (PSD) Product Data. Version 1.1 [Dataset]. UCAR/ NCAR - Earth Observing Laboratory. https://doi.org/10.26023/8HMG-WQP3-XA0X
- Yamaguchi, T., & Feingold, G. (2015). On the relationship between open cellular convective cloud patterns and the spatial distribution of precipitation. Atmospheric Chemistry and Physics, 15(3), 1237–1251. https://doi.org/10.5194/acp-15-1237-2015
- Yang, F., Luke, E. P., Kollias, P., Kostinski, A. B., & Vogelmann, A. M. (2018). Scaling of drizzle virga depth with cloud thickness for marine stratocumulus clouds. Geophysical Research Letters, 45(8), 3746–3753. https://doi.org/10.1029/2018GL077145
- Zelinka, M. D., Myers, T. A., McCoy, D. T., Po-Chedley, S., Caldwell, P. M., Ceppi, P., et al. (2020). Causes of higher climate sensitivity in CMIP6 models. *Geophysical Research Letters*, 47(1), e2019GL085782. https://doi.org/10.1029/2019GL085782
- Zhang, D., Wang, Z., Luo, T., Yin, Y., & Flynn, C. (2017). The occurrence of ice production in slightly supercooled Arctic stratiform clouds as observed by ground-based remote sensors at the ARM NSA site. *Journal of Geophysical Research: Atmospheres*, 122(5), 2867–2877. https://doi.org/10.1002/2016JD026226
- Zhou, X., Atlas, R., McCoy, I. L., Bretherton, C. S., Bardeen, C., Gettelman, A., et al. (2021). Evaluation of cloud and precipitation simulations in CAM6 and AM4 using observations over the Southern Ocean. *Earth and Space Science*, 8(2), e2020EA001241. https://doi.org/10.1029/2020EA001241

KANG ET AL. 26 of 26